

# Photoresist Latent and Developer Images as Probed by Neutron Reflectivity Methods

Vivek M. Prabhu,\* Shuhui Kang, David L. VanderHart, Sushil K. Satija, Eric K. Lin, and Wen-li Wu

Photoresist materials enable the fabrication of advanced integrated circuits with ever-decreasing feature sizes. As next-generation light sources are developed, using extreme ultraviolet light of wavelength 13.5 nm, these highly tuned formulations must meet strict image-fidelity criteria to maintain the expected performance gains from decreases in feature size. However, polymer photoresists appear to be reaching resolution limits and advancements in measurements of the in situ formed solid/solid and solid/liquid interface is necessary. This Review focuses on the chemical and physical structure of chemically amplified photoresists at the lithographic feature edge at length scales between 1 nm and 100 nm. Neutron reflectivity measurements provide insight into the nanometer-scale composition profiling of the chemical latent image at an ideal lithographic line-edge that separates optical resolution effects from materials processing effects. Four generations of advanced photoresist formulations were examined over the course of seven years to quantify photoresist/photoacid and photoresist/developer interactions on the fidelity of lithographic features. The outcome of these measurements complement traditional resist design criteria by providing the effects of the impacts of the photoresist and processing on the feature fidelity. These physical relations are also described in the context of novel resist architectures under consideration for next-generation photolithography with extreme-ultraviolet radiation.

## 1. Introduction

Modern nanofabrication employs electron, ion, and photon beams to pattern thin polymer films that serve as etch-resistant templates for subsequent pattern transfer processing steps. Since the invention of chemically amplified photoresists, features with higher resolution and increased beam sensitivity continue to meet rapid production demands. However, imaging materials

require even further development as feature sizes approach 22 nm. The Rayleigh equation, provides the scaling criteria that predict the smallest optically defined image,<sup>[1]</sup>

$$R = k_1 \frac{\lambda}{n \sin \theta} \quad (1)$$

where  $\lambda$  is the source wavelength,  $n$  the medium refractive index,  $n \sin \theta$  is the numerical aperture (NA) with the incidence angle  $\theta$ , and  $k_1$  is a process-dependent factor. Photoresist technology has evolved from projection lithography that started with the near ultraviolet (UV) that made way for laser sources in the deep ultraviolet (DUV) from KrF ( $\lambda = 248$  nm) to ArF ( $\lambda = 193$  nm). Immersion lithography further decreases the 193 nm wavelength by using water as the immersion fluid and is on track to produce features down to 22 nm half-pitch. Manufacturing tools have taken advantage of the Rayleigh equation to guide transitions from each technological node (smallest feature size) up to diffraction limit. Next-generation materials for sub 22 nm features expect to image 13.4 nm radiation in the extreme ultraviolet (EUV).

While the Rayleigh equation defines the resolution, the ability of the photoresist to perfectly replicate the mask features is a difficult challenge due an image blur that arises from photoacid diffusion. This image blur is the first level of control that must be reduced to achieve the smallest feature sizes or critical dimension (CD). Further, while nominal resolution is reached the presence of line-width variations called line-width roughness (LWR) or line-edge roughness (LER), **Figure 1**, presents an ultimate resolution challenge. LER and LWR must be reduced to less than 2 nm for 32 nm half-pitch as they impact device performance and increased power consumption.<sup>[2,3]</sup> Therefore, the photoresist materials chemistry plays a substantial role for both resolution and LER/LWR in addition to the manufacturing of high-quality optical elements and manufacturing tools with 193 nm immersion lithography and potentially EUV lithography.

### 1.1. Chemically Amplified Photoresists

Photoresist materials convert the optically defined pattern into three-dimensional nanometer-scale features (Figure 1). These

Dr. V. M. Prabhu, Dr. S. Kang, Dr. D. L. VanderHart, Dr. E. K. Lin, Dr. W.-L. Wu  
Polymers Division  
National Institute of Standards and Technology  
Gaithersburg, Maryland 20899, USA  
E-mail: vprabhu@nist.gov  
Dr. S. K. Satija  
Center for Neutron Research  
National Institute of Standards and Technology  
Gaithersburg, Maryland 20899, USA

DOI: 10.1002/adma.201001762

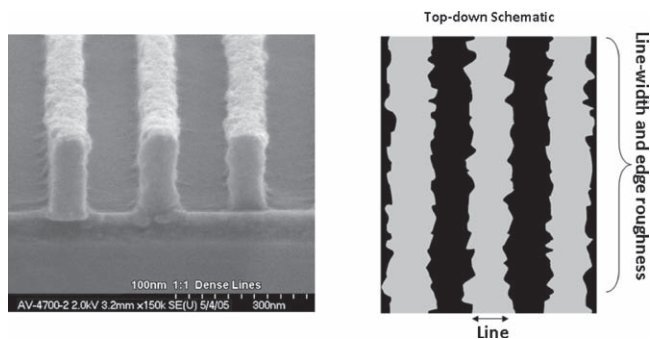


**Figure 1.** Scanning electron microscopy image of the cross-section of 100 nm 1:1 line-space lithographic line made by ArF photolithography. The fluctuations in the feature critical dimension along the line are quantified by line-edge roughness and line-width roughness metrics.

chemically amplified photoresists are formulations of an acid-sensitive polymer film blended with photoacid generators (PAGs) and other additives.<sup>[4,5]</sup> Using a mask, the patterned exposure causes photolysis of the molecularly mixed PAG within the thin film to form photoacids (**Figure 2**). An elevated temperature step called the post-exposure bake (PEB) is then applied and the acidic protons (photoacids) diffuse and catalyze a deprotection reaction on the acid-sensitive polymer to change the local polymer solubility in an aqueous hydroxide solution. The photoacids are catalysts as they are regenerated by each deprotection reaction;<sup>[6]</sup> hence, the term chemical amplification refers to the cascade of reactions that occur within the photoresist induced by a photolysis event. Therefore, these photoresists require fewer photons and hence lower exposure doses to fabricate features and provide the required high throughput of printed wafers in manufacturing.

The quality of the final patterned structures is dependent upon sequential process steps that influence either the spatial distribution of the photoacid or the spatial extent of the photoacid catalyzed reaction-diffusion process. Using interferometric lithography and varying aerial image contrast, Hinsberg et al. demonstrated that the initial photoacid catalyst distribution controlled the printed feature quality.<sup>[7]</sup> Pawloski et al. identified an apparent resolution limit in the final feature quality as quantified by LER<sup>[8]</sup> through a systematic aerial image study. The relationship between the optical exposure quality and the feature quality are correlated to and dependent upon the reaction-diffusion of the photoacid<sup>[9–11]</sup> into the unexposed regions that leads to image spreading or blurring.<sup>[6,12,13]</sup> Controlling the reaction-diffusion process remains the predominant strategy to achieve resolution and feature quality.<sup>[3,14–17]</sup> This becomes important as the feature sizes approach the characteristic photoacid diffusion lengths. Hence, experimental methods that clarify these interactions and transport mechanisms are needed to design next-generation materials for the successful fabrication of structures less than 22 nm.

In principle, photoacid diffusion will not necessarily determine LER if the photoacid is thermodynamically incompatible (phase separated) with the matrix at lower temperatures prior to exposure and PEB. For purposes of this Review article, thermodynamic compatibility of the photoacid and the matrix was demonstrated for a series of PAG/polymer resist pairs used in this study



**Vivek M. Prabhu** is currently Project Leader for Nanoparticle Assembly in Complex Fluids. He received his Ph.D. in Polymer Science and Engineering from the University of Massachusetts-Amherst in 2001 and subsequently joined NIST as an NRC-NIST Postdoctoral Fellow, where in 2003 he led the Polymers for Next-

Generation lithography project. His areas of interest are in polymer physics of thin films and the structure and dynamics of charged nanoparticles and polymers using scattering, reflectivity, and spectroscopic methods.



**Wen-li Wu** is currently a NIST Fellow in the Materials Science and Engineering Laboratory. He received his Ph.D. from the Massachusetts Institute of Technology in 1972 and then joined the research staff at the Monsanto Co.. In 1979 he joined the Polymers Division staff and after 25 years of Service became a Fellow. His primary field of scientific

expertise is the development of advanced X-ray/neutron scattering methods and their applications to investigations of the structure and properties of polymeric materials in thin films and at interfaces.



**Shuhui Kang** is a Guest Researcher in the Polymers Division. He received his Ph.D. in Physics from the University of Massachusetts-Amherst in 2003. His scientific and technical areas of interest are in polymer physics of thin films and the vibrational spectroscopy of polymers.

and materials for 157 nm lithography using solid-state proton spin-diffusion NMR.<sup>[18,19]</sup> These bulk measurements, extendable to ultrathin films,<sup>[20]</sup> show that the specific PAGs mentioned in this paper are thermodynamically compatible with all of the associated polymers cited in this paper as well as a series of molecular glass resists. While the NMR data were on bulk samples rather than thin film samples and employed more volatile solvents than

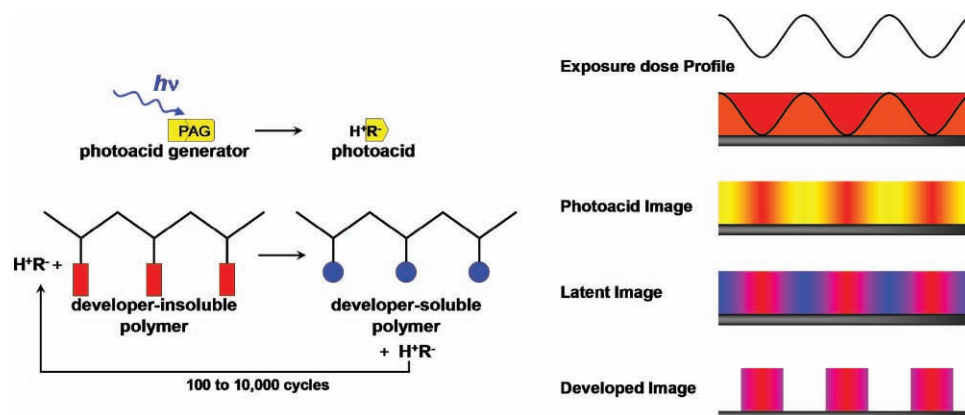


**Figure 2.** Schematic of the photolysis process of a photoacid generator that forms a strong acid ( $H^+R^-$ ) and the subsequent acid catalytic reaction that changes the solubility of the polymer in a developer solution. Schematic of the mask-defined dose profile, subsequent profile in the photoresist film that leads to a photoacid image and chemical latent image formed during the post-exposure bake. The final developed image is formed after selective dissolution in a developer solution as determined by the extent of chemical reaction in the nominally exposed regions.

those used commercially in lithographic applications, the results applied to the question of thermodynamic compatibility. Stoichiometrically relevant photoresist/PAG blended pairs showed that each pair was characterized by a similar, but conservative upper limit of a 4-nm-size scale ascribed to the diameter of a spherical PAG phase with a likelihood of smaller domains. This determination, coupled with the argument that the slow removal of solvent, when casting from the bulk, should result in larger domains if thermodynamically incompatible.

### 1.2. Ideal, Statistical Models

As feature sizes are reduced to below 22 nm a general problem to simultaneously reduce exposure dose, feature critical dimension (CD), and LER was observed experimentally and theoretically. These observations suggest only two of these metrics may be met at the sacrifice of the third. Several models<sup>[21–23]</sup> have been proposed for the scaling of LER with critical parameters as summarized by **Table I**; LER is noted as proportional ( $\propto$ ) to products of each column of parameters.  $D_e$  is the dose at the line-edge (threshold for development),  $\alpha$  is the fraction of light absorbed,  $\epsilon$  is the quantum efficiency defined by the

(molecules of acids produced)/(number of absorbed photons),  $L_d$  is the effective photoacid diffusion length, and LILS is the latent-image log slope.

In the model, the shape of the reaction diffusion front (LILS) appears inversely proportional to LER. However, the shape is actually a modulation of the optical image, such that during the PEB process the optical image is blurred due to photoacid diffusion. While the LILS may be maximized by improving the optical image quality (reducing wavelength, higher NA optics) the blurring process remains resist materials dependent. This is a major limitation, in particular, as the feature sizes are reduced. Therefore choice of photoresist chemistry, PAG size, processing time, and temperature ultimately determines both the LILS and the photoacid diffusion length ( $L_d$ ). The LILS is also coupled to the distribution of generated photoacid and hence, photon exposure distribution. At very low exposure doses ( $D_e$ ) the ability to define a feature with low exposure statistics inherently leads to a poor resolution as covered by Gallatin.<sup>[21,25,26]</sup> For EUV lithography, novel approaches are being developed to maximize the absorbance and quantum efficiency,<sup>[24,27]</sup> since the basic mechanisms differ from DUV exposure.

In order to bridge the gap between the scaling models and more advanced simulations<sup>[12,28,29]</sup> experimental approaches have been developed. **Figure 3** shows the latent image (deprotection profile) in a model poly(methyladamantyl methacrylate) photoresist for 193 nm lithography using neutron reflectivity with an ideal step exposure for two different DUV exposure doses. The specific details will be discussed later, but here the deprotection level scales from 0 to 1, where a deprotection of 1 implies complete loss of the protecting groups. On average, for this system, a deprotection level greater than 40% leads to dissolution (or development) in an aqueous hydroxide developer solution and therefore only a portion of the image will dissolve away. This average composition is also referred to as the solubility switch. The distance from the initial exposure edge to the point of development is a definition of  $L_d$ . Further, the local deprotection slope (LILS) at the solubility switch is coupled to the dose and diffusion length<sup>[30]</sup> as the two profiles are a result from equal PEB time and temperatures.

**Table I.** Scaling of line-edge roughness based upon statistical approaches.

	Dose at exposure threshold ( $D_e$ )	Latent-image log slope (LILS)	Absorbance ( $\alpha$ )	Quantum Efficiency ( $\epsilon$ )	Photoacid Diffusion Length ( $L_d$ )	Ref.
$LER \propto$	$1/\sqrt{D_e}$	$1/LILS$	$1/\sqrt{\alpha}$	$\sqrt{1+\frac{1}{\epsilon}}$	$1/L_d$	[22]
$LER \propto$	$1/\sqrt{D_e}$	$1/LILS$	$1/\sqrt{\alpha}$	–	$1/L_d^{3/2}$	[21]
$LER \propto$	$1/\sqrt{D_e}$	$1/LILS$	–	$\sqrt{\frac{1}{\epsilon}}$	$1/L_d^{3/2}$	[23]
$LER \propto$	$1/\sqrt{D_e}$	$1/LILS$	–	–	$1/L_d^3$	[24]

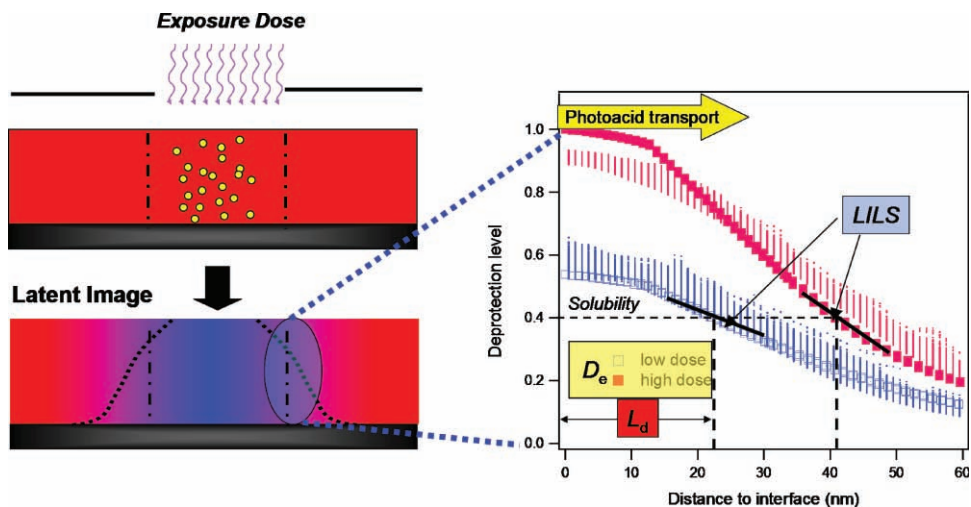


**Figure 3.** Example of three critical variables that currently limit resolution and line-edge roughness.

The chemical details of the photoresist, photoacid, and additives structure are not incorporated into statistical models (Table I), nor are the details of the development process. Since the interfaces are on the nanometer scale, measurements with sufficient sensitivity and resolution are required. Neutron reflectivity techniques have sensitivity and resolution to provide insights regarding the materials by considering an ideal photoresist interface to quantify the composition profile of the latent image and the developed image.

It is arguable which is more important for LER, the initial PAG distribution or the length scale of homogeneity. In a worst-case scenario with PAG domains of 4 nm diameter for a sample with a typical 5 % PAG loading, the mean distance between domains is  $\approx 10$  nm; the effects of inhomogeneous PAG distribution on LER fade for diffusion distances above  $\approx 8$  nm. Most data discussed herein involve PAG diffusion lengths that exceed 8 nm. Another consideration is thermodynamic compatibility of PAG molecules with resist polymers in spite of typical PAG characteristics of strong local polarity, perfluorinated anion, aromatic and ionic character that may produce phase separation, microphase separation, or phase segregation in a primarily aliphatic or aromatic resist matrix. Even for isolated PAG or small clusters of four to eight molecules that sequester, their most incompatible attributes lead to a mean inter-cluster distance in the 5 nm to 6 nm range. Therefore, it is likely that PAG diffusion exceed such lengths during the PEB in order to minimize the influence of initial PAG distribution. However, the influence of exposure dose would play a role in controlling the statistical nature of photoacid generation that could lead to large distances between photoacids.

### 1.3. Ideal Experimental Interfaces

The interface between exposed and unexposed photoresist is of direct interest as shown in Figure 3 and Figure 4. The lithographic line was simplified by flipping the line-edge by  $90^\circ$  to form a planar interface, rather than vertical edge. Thus, by

placing photoacid generator in the top layer of a bilayer structure, the thin film can be flood exposed, post-exposure baked, and developed. This simplified interface was prepared by successive spin-coating of a photoresist film and a second polymer film containing a photoacid generator (in a non-solvent for the first film) to form a bilayer, as shown in Figure 4. This provides a sharp initial photoacid step profile after exposure, since the photoacid is only in the top layer. During the post-exposure bake process, below the glass-transition temperature of the polymer, the photoacid diffuses into the bottom photoresist layer and catalytically cleaves the acid-labile protection group. Lastly, the film is developed by an aqueous base developer and measured for surface roughness that mimic the LER formed at the true lithographic edge.

The above model line edge was used by Lin et al. to first demonstrate neutron reflectivity as a general method to probe the reaction front.<sup>[31]</sup> By using a deuterium-labeled protection group after the reaction the volatile products leave the film and provide the change in contrast necessary to measure the deuterium profile with nanometer resolution. Therefore, the ideal line-edge was blurred by photoacid diffusion to form a smooth composition profile from an initial sharp edge. The model system of Lin et al. is shown in Figure 4 along with the experimental data before and after the PEB step.

This Review is organized as follows: Section 2 provides an overview of the reflectivity methods applied to characterize thin films for in-plane and out-of plane structures. Section 3 highlights the application of neutron reflectivity methods to measure the reaction-diffusion front, or latent image. Further, the materials strategy (polymer chemical composition, photoacid generator size, and amine additives) to control the reaction front are described as well as the effect of processing conditions (reaction temperature and time). The fundamentals developed are tested with full lithographic testing performed at Sematech, a research consortia with international leaders in semiconductor manufacturing. Section 4 highlights the achievements made in testing dissolution process models and structure of the developed image in resist materials using

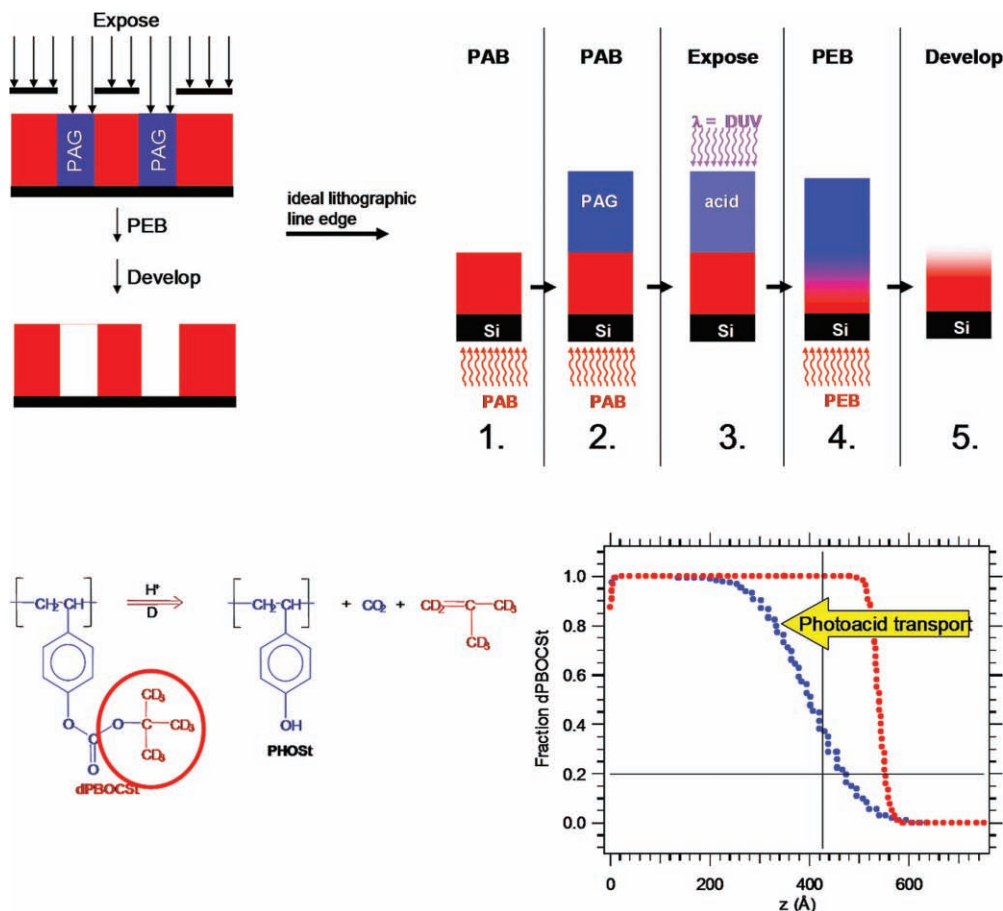


**Figure 4.** Top: Multiple spin-coating method to prepare model lithographic line edge. Bottom: Model 248 nm photoresist based upon poly(hydroxystyrene). The unexposed initial sharp edge represents the transition of the bilayer from 100% dPBOCSt to PHOST containing PAG after the post-apply bake (step 2). After UV exposure (step 3) and a post-exposure bake (step 4) the loss of deuterium protection groups highlight the deprotection reaction caused by photoacid reaction-diffusion to form the diffuse dPBOCSt composition profile.

neutron reflectivity methods. Sections 3 and 4 highlight conventional polymer materials and a few limitations; Section 5 provides a glance at new chemically amplified resist architectures that attempt to resolve fundamental issues associated with polymers. Lastly, the major conclusions are summarized in Section 6.

## 2. Neutron Reflectivity

In any reflectivity experiment using electromagnetic waves (e.g., X-rays, ultraviolet, visible, infrared light) or particle waves (e.g., neutrons) a variation in contrast between the material and the surrounding medium (e.g., air and substrate) is necessary to measure the film structure such as thickness and density. The coherently reflected waves in neutron and X-ray reflectivity are of particular interest because they provide subnanometer resolution due to the wavelengths ( $\lambda$ ) used: 0.154 nm Cu  $K\alpha$  X-rays and 0.475 nm for cold neutrons at the NIST Center for Neutron Research NG7 horizontal reflectometer. The photoresist resolution challenges are in the order of nanometer, so X-ray and neutron reflectivity methods are capable to resolve

the area-averaged density and composition profiles of the latent and developed images.

The refractive index for neutrons and X-rays are typically less than unity by order  $O(10^{-5}$  to  $10^{-6})$  with the complex index,  $n = 1 - \delta + i\beta$ , defined by refractive index and extinction coefficients. Where,

$$\text{X-rays } \delta_X = \frac{N_A \lambda^2}{2\pi} \rho_{el} r_o \quad \text{and} \quad \beta_X = \frac{\mu \lambda}{4\pi}$$

$$\text{neutrons } \delta_N = \frac{\lambda^2 b}{2\pi v} \quad \text{and} \quad \beta_N = \frac{N_A \sigma_a \lambda}{4\pi}$$

$N_A$  is Avogadro's number and for X-rays  $\delta_X$  is sensitive to the molar electron density variations ( $\rho_{el}$ ) multiplied by the classical electron radius ( $r_o = 2.82 \times 10^{-13}$  cm), while  $\mu$  is the linear attenuation coefficient. Neutrons, however, interact with the nucleus and are insensitive to the electron density. The contrast arises from the nuclear coherent scattering length density variations, where  $b/v$  quantifies the total scattering length ( $b$ ) within molecular volume ( $v$ ). The atomic scattering length varies randomly from element to element, however, a large coherent

scattering length difference occurs between hydrogen ( $b_H = -0.374 \times 10^{-12}$  cm) and deuterium ( $b_D = -0.667 \times 10^{-12}$  cm) isotopes. Therefore neutron reflectivity contrast may be enhanced by deuterium substitution to measure composition profiles.  $\sigma_a$  is the neutron absorption cross section. (Of direct interest is the calculation of the scattering length density profile from the measured absolute reflectivity.) Quite often the unit of  $Q_c^2 = 16\pi \sum b_i/v$  is used, which is proportional to the scattering length density defined by the sum of the atomic scattering lengths of a molecule within a molecular volume  $v$ .

### 2.1. Specular Neutron Reflectivity

A neutron reflectivity experiment measures intensity as a function of angle, or wave vector  $q_z = 4\pi\lambda^{-1} \sin\theta$  (see Figure 5) perpendicular to the surface. The absolute reflectivity may be related to the refractive index profile, hence composition and gradients, using classical optics. Since the refractive index is slightly less than unity, the beam is totally reflected if the incidence angle is smaller than the critical angle ( $\theta_c$ ), which is of the order of a fraction of a degree. Near the critical angle the penetration depth of the beam into the material is a few nanometers, and is the reason why grazing incidence techniques are inherently surface sensitive. As the angle of incidence is increased above the critical angle the penetration depth increases and is determined by the absorption of the reflecting material (Figure 5).

For the case of specular reflectivity where the incidence and reflectance angles ( $\theta$ ) are equal, the reflectivity for a single film on a substrate may be calculated exactly. However, for multilayers, the reflectivity is calculated recursively by considering the reflection and transmission at each layer that are defined by a

wave vector and scattering length density dependent Fresnel coefficient. Then the reflection coefficients are calculated iteratively and the total reflection determined through recursive relations from the last to the first layer. Due to the interference of reflected waves a series of fringes of oscillating amplitude are observed that are sensitive to the film thickness. Further, the presence of interfacial broadening dampens the fringe amplitude.

### 2.2. Off-Specular Neutron Reflectivity

In off-specular reflectivity, or diffuse scattering, the average in-plane correlations are measured rather than the average depth profile. This is due to the measurement of the scattering as a function of the rocking angle  $\omega$  around the specular condition (Figure 5). This places a component of the wave vector  $q$  within the  $x$ - $y$  plane. While  $q_z$  remains largely constant during the transverse scans,  $q_x$  is defined as  $q_x = \frac{2\pi}{\lambda} (\cos(2\theta - \omega) - \cos(\omega))$ . This provides a measurement complementary to the composition profiles by measuring the structure or correlation length for rough surfaces or fluctuations at interfaces within the plane of the film. The physics of off-specular reflectivity begins with the Born approximation, followed by the distorted-wave Born approximation (DWBA) as proposed by Sinha et al. for a rough surface of a single substrate.<sup>[32]</sup> There is no difference in the theoretical aspects between X-ray and neutron scattering except the calculation of scattering contrast.

Within the Born approximation, the off-specular scattering amplitude  $A(q)$  is typically modeled as,

$$A(q) \propto \langle \psi_i | \rho(r) | \psi_s \rangle \quad (2)$$

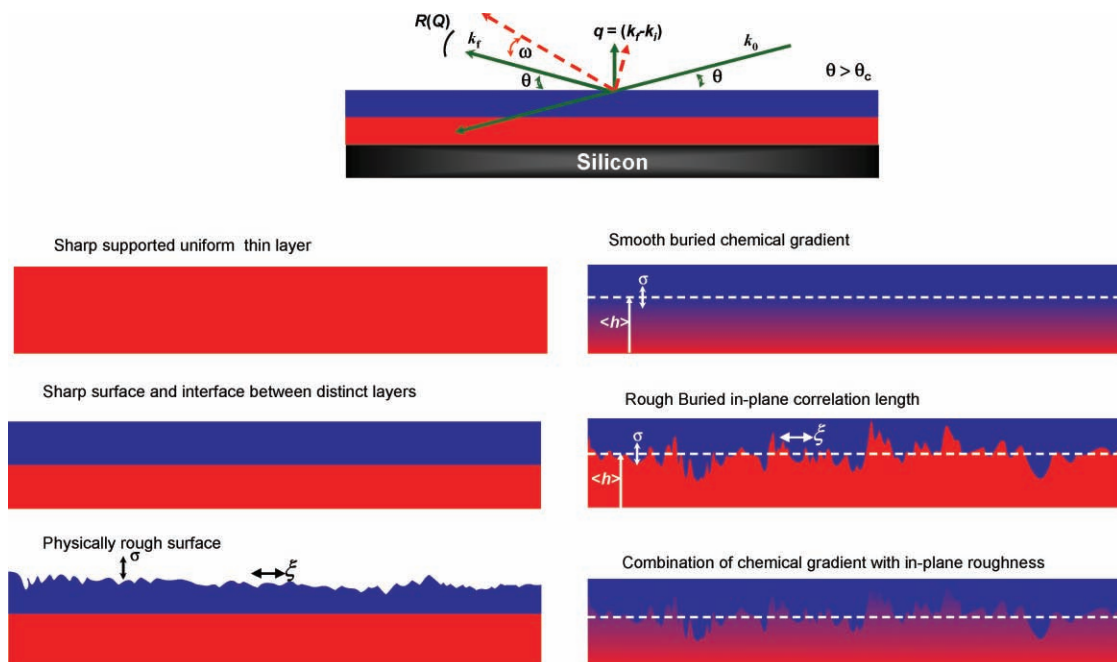


**Figure 5.** Top: Schematic of specular and off-specular reflectivity; the off specular reflectivity measures at a rocking angle  $\omega$  about the specular condition that provides a component the wave vector in the plane of the film. Bottom: Variety of interfacial structure of interest with characteristic surface and buried structure defined by thickness and form of the gradient interfaces and surfaces.

where  $\psi_i$  and  $\psi_s$  represent the incident and time reverse wave functions. Here  $\rho(r)$  is the scattering density function describing the interface topology as well as compositional fluctuations within the medium. Within the Born approximation, the wave functions are plane waves that are independent of the position  $r$ . Therefore, the scattering intensity is simply  $A(q)A^*(q)$ , where  $q = (k_s - k_i)$  is the scattering vector and  $k_i$  and  $k_s$  denote the incident and scattered wave vectors, respectively. When both the incident and the time reverse scattering wave functions are approximated as plane waves, Equation (2) represents a Fourier transform of the scattering density function.

In practice, the interface may consist of both surface roughness and compositional fluctuations (Figure 5). In this case, the diffuse scattering may be analyzed using a modified distorted-wave Born approximation.<sup>[32,33]</sup> This description models the self-affine interface with a roughness amplitude of  $\sigma$ , a lateral correlation length ( $\xi$ ), and a Hurst parameter ( $H$ ). The diffuse scattering from multilayer stacks was analyzed using the approach of Wormington et al.,<sup>[33]</sup> with the in-plane correlations described by

$$C(x, y) = \sigma^2 e^{-\left(\frac{\sqrt{x^2 + y^2}}{\xi}\right)^{2H}} \quad (3)$$

The approach of Wormington et al.,<sup>[33]</sup> models the structure factor  $\rho(r)$  as a multilayered structure and both compositional fluctuations and roughness included explicitly at each interface. The wave functions  $\psi_i(r)$  and  $\psi_s(r)$  at each layer are calculated using a typical specular reflectivity fitting algorithm. By combining specular and off-specular techniques one may distinguish different forms of buried interfacial structure as suggested by Figure 5. The intensity of off-specular neutron reflectivity due to buried interfaces may be enhanced by deuterium labeling.

### 3. Reaction-Diffusion Fronts

Advanced photoresist formulations rely on the photoacid catalytic chain that amplifies a single PAG photolysis event. Each photoacid may produce thousands of deprotection events upon the acid-sensitive polymers. The loss of volatile protection groups changes the polarity of the polymer film such that above an average deprotection level (solubility switch) the film becomes soluble in an aqueous hydroxide developer. The model line-edge approach (Figure 4) developed by Lin et al.<sup>[31]</sup> first demonstrated neutron reflectivity as a general method to probe the reaction front of photoresists for 248 nm lithography. The loss of the deuterium-labeled *tert*-butoxycarbonyl (tBOC) groups provided the change in scattering length density contrast, such that the deuterium profile accurately represents the chemical latent image. In that case the ideal line-edge showed a composition profile broadened by photoacid diffusion from the initial sharp edge. The basic shape of the reaction-induced chemical front identified that the spatial extent can impose resolution limits. Therefore tools that could estimate the

spatial extent, with nanometer resolution were necessary. The influence of chemical reaction time, photoacid generator size, photoresist copolymer chemistry is highlighted.

#### 3.1. Influence of PEB Reaction Time

Once feature sizes reached sub-100 nm DUV lithography shifted from 248 nm to 193 nm wavelengths. At 193 nm, aromatic polymers had too high absorption and therefore an entirely new photoresist polymer platform was required. The resist community developed novel monomers, with low absorption at 193 nm, such as the fused-ring structure of methyladamantyl methacrylates. In the case of poly(methyladamantyl methacrylates) (PMAdMA) the adamantyl protecting group is cleaved to form methylene adamantane (MA) and poly(methacrylic acid) (PMAA) as shown in Figure 6.

This MA is less volatile than the tBOC deprotection products (isobutene and CO<sub>2</sub>), but partially leaves the film as can be measured quantitatively by Fourier transform infrared spectroscopy (FTIR). Importantly, the deprotection leads to the base soluble poly(methacrylic acid). The bilayer in this case used PAG in poly(hydroxystyrene) (PHOST) as the top layer identical to the work of Lin et al. The fact that at elevated temperature the MA group leaves, provides sufficient neutron scattering length contrast through the proton density changes. While not an ideal situation, in order to improve the uniqueness of the fitting algorithms, neutron reflectivity was combined with FTIR to provide a component balance that restricts the fits. With this approach the composition profiles of PMAdMA, MA, and PMAA were resolved.<sup>[34–36]</sup>

Figure 7 a shows neutron reflectivity data for PHOST/PMAdMA bilayers containing di-*tert*-butylphenyl iodonium perfluorooctane sulfonate (DTBPI-PFOS) PAG in the acid-feeder layer offset as a function of PEB times at 130 °C. The periodicity of the reflectivity fringe wavelength and amplitude indicates the bilayer structure is composed of layers with distinct scattering length densities. The reflectivity data fits are shown by the solid lines. The corresponding neutron scattering length density profiles are in Figure 7b. The scattering length density profile begins in air at zero, increases to the value of PHOST, and then decreases to the value of PMAdMA. The substrate is then encountered with scattering length densities corresponding to the silicon oxide layer and silicon. As the PEB time is increased, the  $Q_c^2$  of the PMAdMA layer near the PHOST increases due to the loss of hydrogen content from acid catalyzed deprotection and the partial volatilization of the methylene adamantane.

The  $Q_c^2$  profile from Figure 7b cannot be directly interpreted as the deprotection profile due to the presence of residual

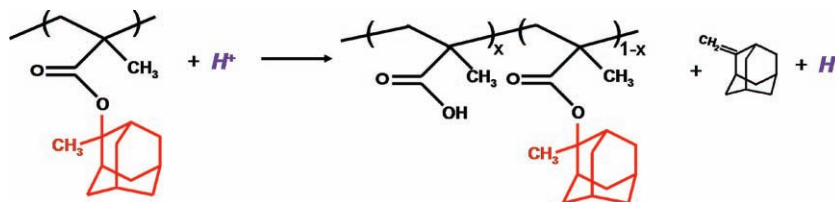
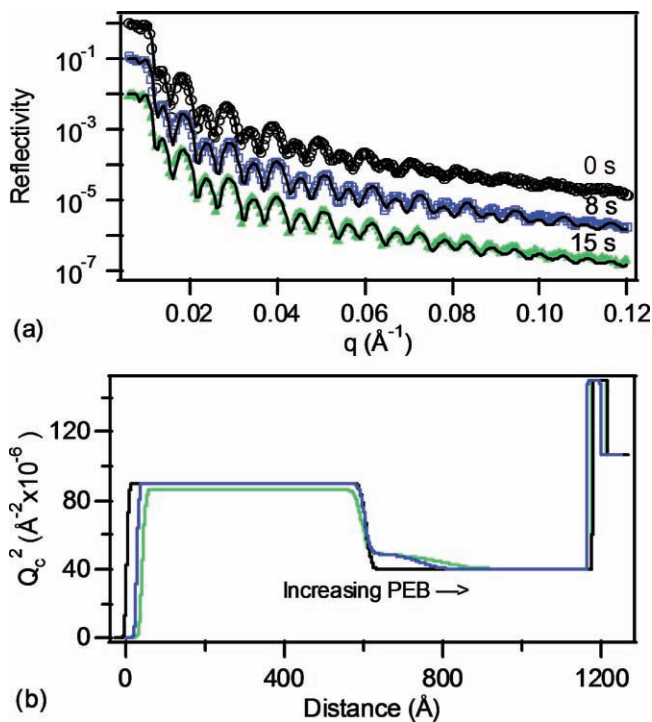


Figure 6. Photoacid catalyzed deprotection reaction of poly(methyladamantyl methacrylate).



**Figure 7.** a) Neutron reflectivity profiles for bilayers of PHS (+ DTBPI-PFOS) and PMAdMA with (○) 0 s, (◻) 8 s, (▲) 30 s PEB at 130 °C. Two distinct beatings are evident in the data due to the scattering length density contrast between PHS and PMAdMA. The best fits of the reflectivity are shown by the solid lines corresponding to (b) the scattering length density profile. The scattering length density of the PMAdMA layer increases with PEB time due to loss of hydrogen content (methylene adamantane). Reprinted with permission.<sup>[34]</sup> Copyright 2006, American Chemical Society.

methylene adamantane after deprotection. The reflectivity data can be fit by considering the volume fraction profiles ( $\phi_i$ ) of the individual components with known scattering length density ( $Q_{c,i}^2$ ). For the specific case examined here we have the following expressions,

$$Q_{c, \text{film}}^2(z) = \phi_{MA}(z) Q_{c, MA}^2 + \phi_{MAA}(z) Q_{c, MAA}^2 + \phi_{MAdMA}(z) Q_{c, MAdMA}^2$$

$$\phi_{MAdMA}(z) = 1 - \phi_{MA}(z) - \phi_{MAA}(z) \quad (4)$$

FTIR measurements provide the average quantity of deprotection products ( $\phi_{MA}$ ) that remain in the film and the average deprotection level designated by  $\phi_{MAA}$ . These independent values serve as restrictions to compare the integrated concentrations of MA, MAA, and MAdMA within the films determined by neutron reflectivity through the measurement of  $Q_{c, \text{film}}^2(z)$ . The component profiles ( $\phi_{MA}$ ,  $\phi_{MAA}$ ) are determined using Equation (4) by assuming that PMAdMA is completely deprotected at the interface with the acid feeder layer upon PEB and then allowing the deprotection profile to decay smoothly. The characteristic decay length is varied to minimize the differences in deprotection and MA amounts between FTIR and NR measurements. To obtain the best fit, the scattering length density of the deprotected

region is changed slightly from the previous fit and only the width and thickness of the deprotection region are allowed to vary until the difference in concentration between neutron reflectivity and FTIR is less than 3% for all components.

Figure 8 shows the deprotection profiles for four PEB times at 130 °C. The general shape is not described by Fickian diffusion. Therefore, the time-dependence of the reaction is strongly influenced by the interaction between the diffusing photoacid and changing medium. At reaction times longer than 15 s the extent of reaction becomes pinned and the tail of the reaction extent slowly increases. Pinning of the reaction front occurs near a photoacid diffusion length of 200 Å shown by the vertical lines that correspond to the solubility switch. In this case, the reaction rate becomes suppressed; however, the presence of photoacid and the broad tail shows that the reaction does proceed. Houle et al. demonstrated through experiment and stochastic modeling that the mobility (or diffusivity) of the photoacid varies widely in the pure protected and deprotected components.<sup>[12,28]</sup> Therefore, the diffusion-pathway of the reaction could be slowed down simply by the difference in photoacid mobility. Similarly, Willson et al. concluded that the diffusing front of photoacid slows down in the presence of the deprotection products, using a series of photoacid generators.<sup>[16,37]</sup> Therefore, while there is a gradient in photoacid, the presence of a deprotection gradient inhibits the further transport behind the reaction front.

Motivated by these studies, a systematic study of the reaction kinetics of PMAdMA with TPS-PFBS<sup>[30]</sup> was performed with FTIR. In this case a phenomenological model was developed that includes a photoacid loss process, or acid-trapping event, dependent upon the extent of the reaction. The photoacid trapping process was first order in the photoacid concentration ( $H^+$ ) and deprotection concentration ( $\phi_{MAA}$ ). This was further tested as a function of different copolymer compositions, dose, and post-exposure bake temperatures. This limiting model provides some insight into the shape of the deprotection profiles. In the case of Houle<sup>[28]</sup> the decrease in the diffusivity of the photoacid can be modeled as a reversible reaction between the photoacid and the pendent hydroxyl group of the deprotected monomer.<sup>[38]</sup> Houle et al. were able to predict the shape and extent of the deprotection front<sup>[12,28,38–42]</sup> as confirmed through direct measurements by neutron reflectivity.<sup>[31]</sup>

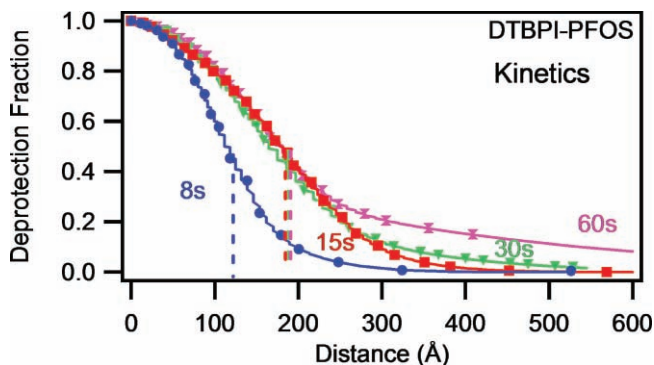


**Figure 8.** a) Deprotection profiles for DTBPI PFOS with PEB at 130 °C for (●) 8 s, (■) 15 s, (▼) 30 s, and (▣) 60 s. The vertical dashed lines correspond to the developed thickness using 0.26 N TMAH. Adapted with permission.<sup>[34]</sup> Copyright 2006, American Chemical Society.

Based upon the initial qualitative interpretation of the reaction-diffusion front for PMAdMA, it appears as though the detailed model for PHOST<sup>[28]</sup> also applies to PMAdMA. However, it is unclear if there is a specific binding between the photoacid and the MAA, or simply reduced diffusivity in the vicinity of MAA-rich regions. Nonetheless, this mechanism can explain the self-limiting effect of deprotection reaction with PEB time in PAG-loaded PMAdMA films.<sup>[43]</sup> The approach utilizes a limited number of parameters sufficient to describe the reaction-diffusion process in this system. By including the trapping mechanism into a simple reaction-diffusion model, the following differential equations are derived assuming constant photoacid diffusivity.

$$\frac{d\phi(x, t)}{dt} = k_p(1 - \phi)H(x, t) \quad (5)$$

$$\frac{dH(x, t)}{dt} = D \frac{d^2 H(x, t)}{dx^2} - k_T H(x, t)\phi(x, t), \quad (6)$$

where  $\phi(x, t)$  and  $H(x, t)$  are the deprotection level and acid concentration respectively,  $D$  is the diffusion coefficient of the photoacid and  $k_p$  and  $k_T$  are the reaction and the acid trapping rate constants respectively. We neglect the effect of the residual MA to simplify the modeling calculations. Previously determined rate constants<sup>[44]</sup> ( $k_p$ ,  $k_T$ ) from single-layer experiments were used to determine the photoacid diffusion coefficient through the PMAdMA by fitting the deprotection profiles for the bilayers using TPS-PFBS. Unlike the case of PHOST, we find that the photoacid trapping does not need to be modeled as a reversible reaction to describe the data. We speculate that the greater ionizability of the methacrylic acid in comparison to hydroxystyrene leads to stronger binding of the photoacid in the deprotected polymer matrix. Despite the assumptions in Equation (5) and (6), the apparent diffusion coefficient for the photoacid is within a factor of two of measurements for PFBS in other fully protected systems,<sup>[28]</sup> approximately  $6 \times 10^{-13} \text{ cm}^2 \text{ s}^{-1}$ . Moreover, the self-limiting reaction-diffusion front can be qualitatively predicted. Figure 9 shows calculated profiles using reaction parameters for a slow, strong photoacid ( $k_p = 30 \text{ nm}^3 \text{ s}^{-1}$ ;  $k_T = 0.4 \text{ nm}^3 \text{ s}^{-1}$ ;  $D = 1 \times 10^{-13} \text{ cm}^2 \text{ s}^{-1}$ ).

The basic shape and limited reaction front is captured by the photoacid trapping process by the deprotection products and highlights the importance of photoresist/photoacid interactions. These interactions play a role in controlling the LILS as well as limiting the photoacid diffusion length. Therefore, materials that strongly interact with the photoacid after deprotection self-limit the photoacid reaction-diffusion front as shown in Figure 8. An investigation into the influence of photoacid size is a natural extension, because increased photoacid size will lead to reduced diffusivity. However, the combined effect on shape of the reaction front (LILS) and diffusion length was not measured.

### 3.2. Photoacid Generator Size Effect

The diffusion length of photoacid generators may be controlled by increasing the size of the super acid such as in the series

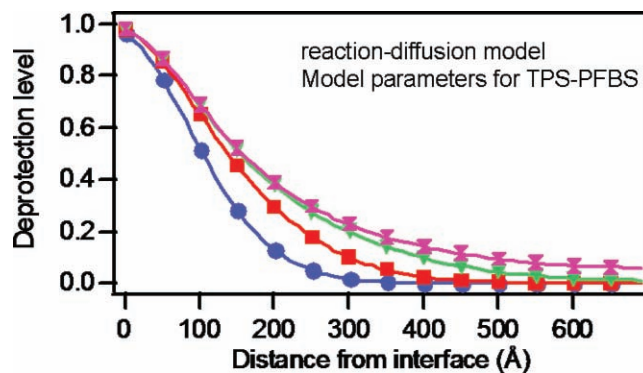


**Figure 9.** Simulated deprotection profiles at a reaction-diffusion front using Equation (3) and (4) for PEB of (●) 8 s, (■) 15 s, (▼) 30 s, and (⊠) 60 s. The front is self-limiting and increasing the bake time only increases the background deprotection. Reprinted with permission.<sup>[34]</sup> Copyright 2006, American Chemical Society.

triflic acid (Tf), perfluorobutane sulfonic acid (PFBS) and perfluorooctane sulfonic acid (PFOS).<sup>[34]</sup> At equal PEB temperatures and reaction time, the smaller photoacid induced a larger extent of reaction and spatial-extent from the ideal line-edge as shown in Figure 10. While the average reaction extents may easily be measured by FTIR, the spatial-extent is missing. By increasing the molecular mass of the photoacid from Tf to PFBS, one maintains a super-acid, but drastically reduces the diffusion of the photoacid and increasing the size further to PFOS the diffusion length is shortened further, but simultaneously the local slope of the deprotection profile is increased. This simultaneous increase in the LILS is crucial to reduce line-edge roughness.

In concept one may further reduce the photoacid diffusion length by covalently bonding the perfluoroalkyl sulfonate to the polymer. In this case the acidic proton may diffuse, but within constraints due to electro-neutrality of the immobile counteranion.<sup>[45]</sup> Even so, by covalently bonding the PAG to the resist the LER and LWR persist, therefore simply limiting the diffusion length is not sufficient. The statistical models of Table I consider that as  $L_d$  is reduced the LER increase for a fixed LILS. However, experimentally, the LILS increases as the  $L_d$  was reduced and therefore are not independent. This highlights the importance of developing materials relationships to the critical lithographic parameters.

The profiles of Figure 10 illustrate the importance of photoacid diffusion and LILS limits. Even with an ideal step-exposure line edge the photoacid induced a blurring of the intended image at the deprotection profiles. A 1:1 line/space feature may be reconstructed using these profiles. As an example for the PFOS case, Figure 11, three different CDs, 130 nm, 90 nm, and 45 nm, are reconstructed. Under the ideal exposure conditions the presence of a sharp LILS and finite  $L_d$  leads to loss of a small fraction of the CD in the case of 130 nm line/space. However, as the CD is decreased down to 45 nm nearly 50% of the intended CD is lost due to photoacid diffusion. Therefore, the smallest feature that may be printed will be bounded by approximately  $\text{CD} \approx 2 \times L_d$ . This can be tested using the bilayer approach and screened for numerous photoresist formulations.<sup>[46]</sup> This problem is compounded because the

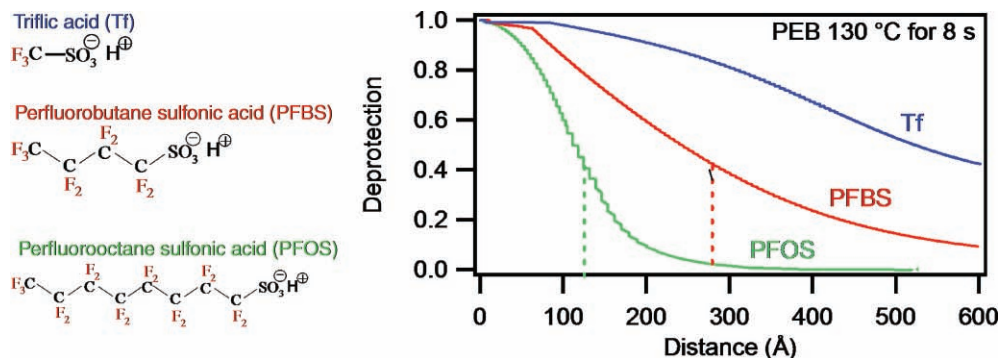


**Figure 10.** Deprotection profiles for model bilayers with 8 s PEB at 130 °C using different PAGs. The dashed lines indicate the solubility switch, determined from development with 0.26 N TMAH. As the PAG size increases, the breadth of the deprotection profile decreases. The largest PAG (DTBPI-PFOS) has a much sharper deprotection profile and shorter deprotection propagation in the film compared to the other PAGs. Reprinted with permission.<sup>[34]</sup> Copyright 2006, American Chemical Society.

finite LILS and  $L_d$  leads to LER that can be of the same order in magnitude of the CD. The roadmap for semiconductors requires that LER ( $3\sigma$ ) comprise no more than 8% of the CD.

The  $L_d$  may be estimated without neutron reflectivity,<sup>[46,47]</sup> however, the shape of the profile is critical, in particular, as the feature size approach the diffusion length. This is the ultimate challenge in photoresists and the effect is controlled by the polymer chemistry as shown next. The statistical scaling of Table I shows that line-edge roughness is inversely proportional to the photoacid diffusion length. Hence, materials are needed that maintain high reaction rates while reducing the photoacid

diffusion length through enhancing the self-limiting diffusion processes. The hydrogen bonding characteristics of photoresists provides a route to reduce the transport properties, but also to increase the glass transition temperature in thin films. Such high glass transition materials are therefore desirable, not only from mechanical stability of the features, but also in the control over transport properties.

### 3.3. Copolymer Composition

Typically photoresists incorporate different comonomer groups to improve imaging capabilities, etch resistance, transparency and development contrast. The hydrophilicity of comonomers have a significant impact on the image quality.<sup>[48]</sup> Here we examine the influence of a non-reactive  $\alpha,\gamma$ -butyrolactonemethacrylate (GBLMA) comonomer incorporated onto the PMAdMA resist polymer. Incorporation of lactones in the polymer improves the imaging<sup>[49–51]</sup> in terms of resist sensitivity to PEB, development contrast, and LER. However, the influence of GBLMA on the photoacid diffusion and LILS has not been examined in detail.

The deprotection profiles determined by neutron reflectivity are shown in **Figure 12** for three different levels of GBLMA copolymer content. As the GBLMA content is increased, the maximum potential deprotection is decreased accordingly. The deprotection level is the fraction of the total polymer converted to the deprotection product, MAA in this case. This explains the vertical offsets between the copolymers and homopolymer. However, the presence of the GBLMA substantially increases the LILS and reduces the photoacid diffusion length. Both copolymers display sharper deprotection fronts at the solubility switch noted by the vertical lines.

This change in the spatial extent of deprotection can be attributed to the decrease in the local diffusivity of the photoacid in the vicinity of GBLMA that leads to a sharper profile. In a complementary set of FTIR measurements the diffusivity of PFBS was determined to be an order of magnitude less in GBLMA than in MAdMA. Incorporation of comonomers of GBLMA thus reduces the initial photoacid diffusivity through the interaction of the acid with the polar GBLMA. Further,

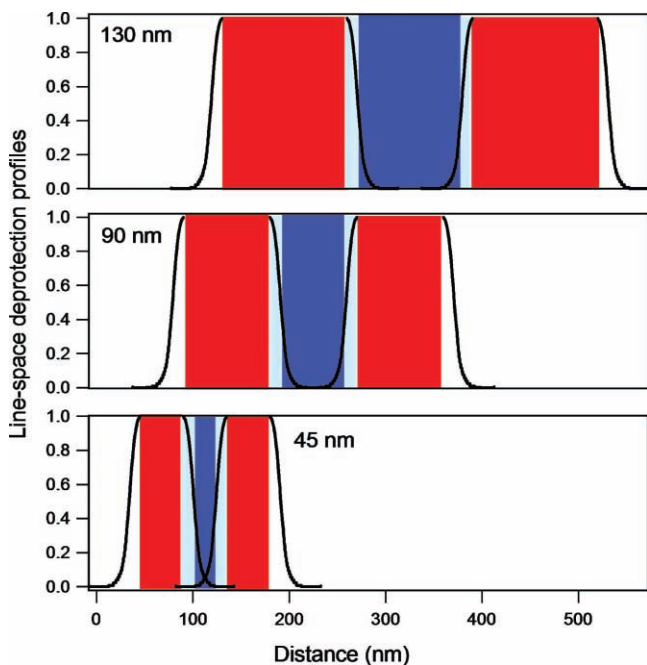


**Figure 11.** Line-space structure as a result from an ideal square-wave exposure profile for the line formed by the PFOS system in PMAdMA. The finite reaction-front width leads to a constant bias to smaller features printed given three different hypothetical line spaces from 45 nm, 90 nm and 130 nm line/space. The effect of acid diffusion will eventually blur-out the line completely for smaller features than  $\approx 2 \times L_d$ .

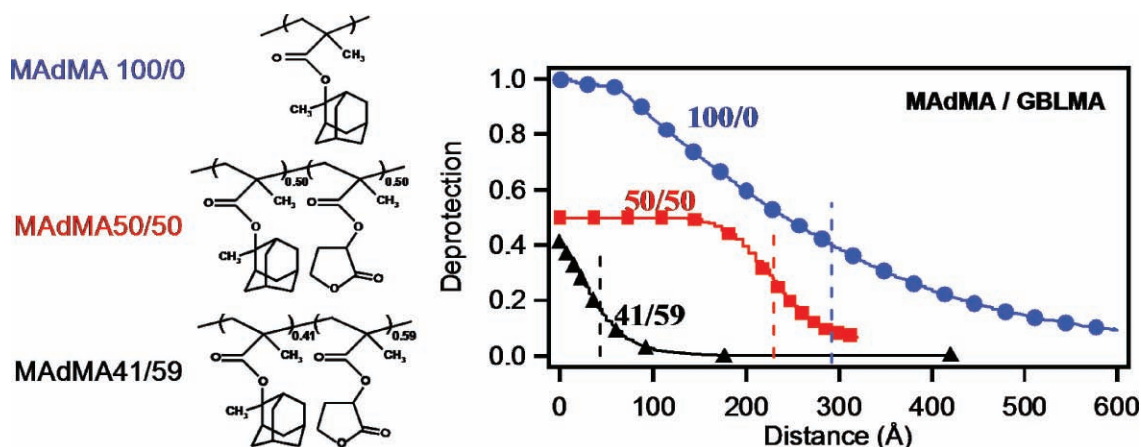


**Figure 12.** Chemical structures of three photoresists used in this study. Left: PMAdMA; middle: P(MAdMA50-co-GBLMA50); right: P(MAdMA41-co-GBLMA59). Latent image after 8 s PEB at 130 °C of three different photoresist copolymers that vary in composition with an inert monomer group. The dashed lines mark where the image is developed in 0.26 N TMAH. Reprinted with permission from SPIE.<sup>[52]</sup> Copyright 2007, SPIE Digital Library.

lactones play a basic role in controlling photoacid diffusion that results in higher LILS.

Therefore, it is not surprising that the deprotection front is dependent upon copolymer composition; however insight into the controlling mechanisms that influence the photoacid diffusion is applicable to design of future photoresists. GBLMA and hydroxystyrene (HOST) are both seemingly inert (unreacting) comonomers in photoresist formulations, but appear necessary for high-quality lithographic imaging.<sup>[9]</sup> Both are more hydrophilic than protected constituents of resins, but only poly(hydroxystyrene) is soluble in aqueous base developer. The solubility of water within homopolymers of GBLMA and HOST is a good measure of their hydrophilicity; a negligible concentration of water is absorbed by P(GBLMA), while at equilibrium PHOST contains nearly 30% water by volume.<sup>[53]</sup> Given the lack of water solubility in GBLMA, it is surprising that the incorporation of GBLMA would dramatically improve the dissolution characteristics of 193 nm resists. The copolymer clearly influences more than simply dissolution properties of the resist as observed in the measurements of the reaction-diffusion fronts. Therefore copolymer structure and architecture are critical to advanced resist materials.

The incorporation of the GBLMA reduces the glass transition temperature from greater than 210 °C for PMAdMA to 162 °C and 172 °C for 50% and 59% GBLMA, respectively. Therefore, even though the processing temperature is further from the  $T_g$  a larger spatial extent of acid diffusion was observed in PMAdMA therefore stressing the importance of photoacid / comonomer interactions in addition to more traditional thermal properties.

### 3.3.1. 193 nm Photolithography at Sematech

The model studies provide a quantitative method to compare different photoresist materials and novel architectures. The copolymer composition effect can be directly tested through lithographic printing at 193 nm. Three photoresists were patterned via 193 nm lithography at Sematech, a research consortia of major semiconductor manufacturers,<sup>[54]</sup> in order to

compare the results from laboratory based fundamental experiments. The optimal exposure conditions for 100 nm line/space features are shown in **Figure 13** for three resist formulations at three different PEB conditions; the LER (nm, 3  $\sigma$ ) along with the corresponding dose-to-size and critical dimension are provided. The PEB of 130 °C with two bake times were chosen to make direct comparisons to the fundamentals.

The MADMA protection content was reduced by increasing the GBLMA and HAdMA content. For a fixed PEB 130 °C for 60 s, the LER decreases from 10.4 to 4.2 nm at fixed PEB conditions. Therefore by changing the polymer chemistry an improvement in the imaging characteristics was observed. At best focus for a fixed dose-to-size of CD = 100 nm the LER was reduced by more than a factor of 2, greater than the square-root dose dependence from Table I. This is because the polymer chemistry influences the reaction kinetics constants that govern the latent image.

Based upon the latent image, by increasing the lactone content the deprotection profile becomes sharper (Figure 12), which after standard development with 0.26 mol L<sup>-1</sup> TMAH leads to lower LER as found by the Sematech data (Figure 13). The polar GBLMA interacts with the photoacid to reduced diffusivity. While the latent image data for the 37% HAdMA containing resist are not available, we speculate that the HAdMA group further interacts with the photoacid to reduce the mobility via the polar hydroxyl group. A FTIR approach has been developed to characterize the spatial heterogeneity in composition of the above photoresist series.<sup>[55,56]</sup> Therefore we may expect compositional heterogeneity also contribute to LER.

Further, the effect of PEB time at 130 °C does not show a large effect on LER for all three resists. This was not surprising primarily due to our observations that the diffusion of the photoacid generator becomes trapped or arrested by the deprotection products (MAA) in particular for the slower diffusing PAGs, TPS-PFBS and DTBPI-PFOS. This led to the pinned deprotection front such that by comparing increasing PEB times, the propagation of the front was significantly slower than that predicted by a diffusive process as discussed in the effect of copolymer composition. However, at longer PEB times

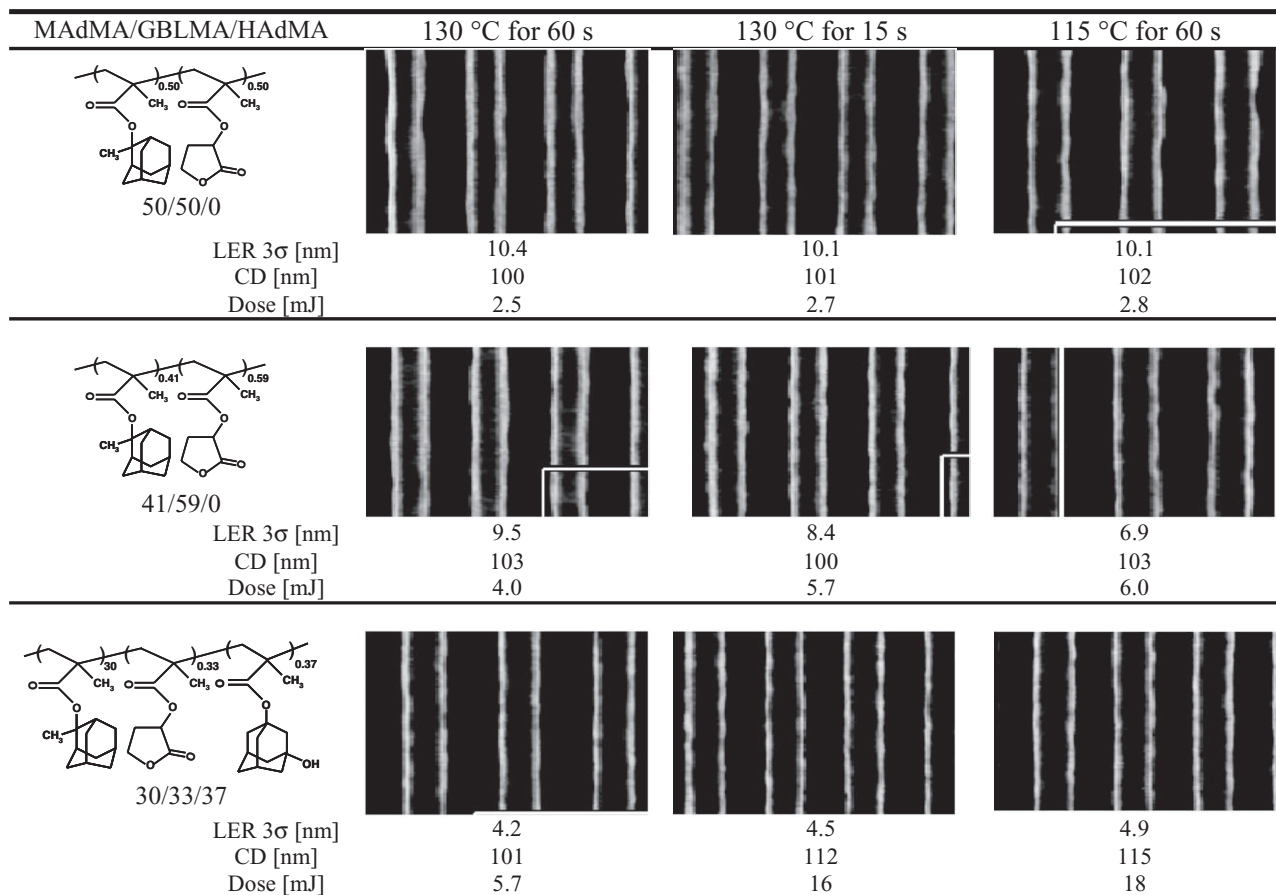


**Figure 13.** Lithographic results for three different photoresist copolymer contents. The formulation consisted of polymer, 5% TPS-PFBS PAG by mass of the polymer, and 10% trioctylamine by mol of PAG.

the latent image width becomes broader and implies increased roughness. This effect may be responsible for the increase by 1 nm in roughness for the 41/59 resist. The formulations all contained 10% by mol of trioctylamine (TOA), as discussed in the next section the amines provide additional control over resolution, photoacid diffusion and LILS.

### 3.4. Effects of Amine Quencher

An effective approach to control photoacid diffusion into the unexposed regions is by the addition of amine bases to the photoresist thin film. In the most simplistic view the presence of amines titrates (or quenches) photoacids that diffuse outside of the nominally exposed regions. In doing so, the spatial-extent of the reaction-diffusion process is controlled. However, the presence of amines also quenches photoacids within the exposed regions leading to a loss in exposure-dose sensitivity of the photoresist. Nevertheless, added base quenchers are an effective method to reduce LER.<sup>[57]</sup> **Figure 14a** shows a hypothetical concentration profile of PAG at an ideal exposure line edge with the horizontal dashed line are equivalents of an amine base. As long as the equivalents of amines are lower than acids one expects to observe photoacid catalyzed reaction in the uniform case. Further, as acids diffuse into acid-free regions the

low levels of acid are effectively titrated because the equivalents of base are greater than the expected low levels of acids. Alternatively, one may impose base only in unexposed areas as in the schematic of **Figure 14b** and therefore maximize the bulk reaction and minimize the influence of acid diffusion. These two cases were quantitatively measured by neutron reflectivity, along with a third case of amines blended with the photoacid generator called coupled acid-base.<sup>[35]</sup>

The mechanism of how an amine reacts with an acidic proton in a solid thin film will be dependent upon the mobility and reactivity. Proportional neutralization<sup>[40,42]</sup> is an ideal case whereby the acid is eliminated from the reaction and the concentration of effective acids is reduced by the stoichiometry. Alternatively, there may be a competitive neutralization whereby an equilibrium is established such that acid-base neutralization occurs in competition with the deprotection reaction.<sup>[40,42]</sup> The experimental data presented here can only speculate which process is more dominant under a given base loading condition since the deprotection profiles are measured, which is not a direct measure of the photoacid distribution.

#### 3.4.1. Uniform Amine Distribution Across Line-Edge

Using the PMAdMA system (**Figure 6**) and TPS-PFBS photoacid generator a comprehensive study of the uniform amine

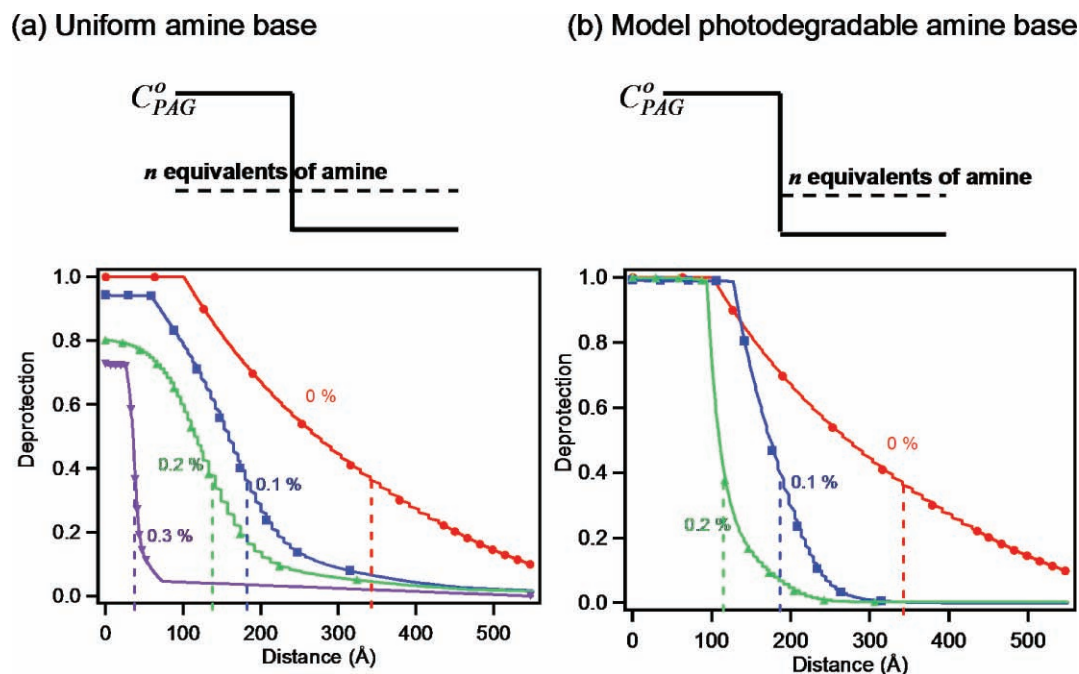


**Figure 14.** Two strategies of amine quencher loading: a) uniform loading in bilayer and b) model photodegradable base, where the base is only in the PMAAdMA bottom layer. The deprotection profiles were measured with different base concentrations (●) 0%, (■) 0.1%, (▲) 0.2%, and (▼) 0.3% by mass of PAG at a fixed PEB at 130 °C for 15 s. The vertical dashed lines indicate the thickness to which the film dissolves when developed for 60 s in 0.26 mol L<sup>-1</sup> TMAH. The symbols apply to both (a) and (b). Reprinted with permission.<sup>[35]</sup> Copyright 2007, American Institute of Physics.

quencher loading was examined.<sup>[35]</sup> A single 130 °C PEB temperature for 15 s is highlighted in Figure 14a. A series of concentrations of the base trioctylamine (TOA) was added at PAG to base molar ratios of 31:1, 15:1 and 10:1, or equivalently 0.1%, 0.2%, and 0.3% mass fractions of TOA. Figure 14a shows the effects of amines at controlling the spatial-extent, LILS, and average reaction extent. The presence of uniform TOA concentration decreases the maximum level of deprotection at the interface with the acid feeder layer; this result is consistent with a decrease in the acid concentration diffusing into the PMAAdMA, either from proportional or competitive neutralization. Additionally, the effective photoacid diffusion length decreased as observed by the confined propagation of the deprotection front. Further, the interface between deprotected and fully protected polymer is sharpened with increasing base concentration; consistent with the statistical neutralization of the diffusing photoacid. At the leading edge of the deprotection front, neutralization of the acid will be favored due to the low concentration of acid relative to the base. The sharp rise in photoacid concentration closer to the acid feeder layer soon overwhelms the presence of base. The resultant photoacid profile after partial neutralization by base should be considerably sharper than the profile without base as can be seen experimentally between the 0% base loading and base-containing profiles. This sharp acid profile is primarily responsible for the sharpening of the deprotection front as the TOA concentration is increased. Using the concepts developed previously, a high deprotection level and sharp profile can decrease diffusion of the photoacid<sup>[35,58]</sup> and limit both propagation and broadening of the deprotection front.

### 3.4.2. Amine Acting as a Model Photodegradable Base at Line-Edge

By placing the amine quencher in the PMAAdMA layer the base is now in a concentration gradient that opposes the photoacid gradient. Comparison of the uniform base case (Figure 14a) and the model photodegradable base (Figure 14b) clearly shows nanometer-scale control of the deprotection profile for two levels of amine quencher at equivalent PEB processing conditions. Each amine quencher strategy reduces the effective photoacid diffusion length. However, importantly, increasing the TOA concentration sharpens the deprotection front with the model photodegradable base resulting in the sharper LILS of the two interfaces.

One specific difference is the level of deprotection at the initial line edge. The model photodegradable base leads to a complete deprotection over the first 100 Å from the initial line edge. Therefore, the photoacid catalytic activity is not sufficiently influenced by counter-diffusion of the base. For the case of uniform base, the deprotection at the interface decreases with addition of TOA. We speculate that this behavior is due to the availability of photoacid in the feeder layer; for the uniform quencher case, the photoacid can be neutralized prior to diffusion into the PMAAdMA, while this option does not exist for the later. The higher deprotection at the initial line edge acts to limit photoacid diffusion that leads to the sharper profile. Therefore the photoacid trapping effect by the deprotection products further controls the LILS.

Trioctylamine is relatively hydrophobic due to the alkyl groups; however, a variety of amine quencher additives are

available with variable hydrophobicity through use of hydroxyalkyl or alkoxyalkyl groups. The general hydrophobicity and size of the amine quencher could further reduce photoacid diffusion. Houlihan et al. proposed that the amine quenchers may segregate or partition into the protected and deprotected domains during the PEB<sup>[59]</sup> depending on the relative hydrophobicity. Further, the reactivity with the photoacid may be controlled by the  $pK_a$  of the amine.<sup>[59]</sup> While lithographic evidence is present on some photoresist/quencher pairs the general relationship between transport of amine quenchers and preferential segregation are poorly understood.

However, even with the ideal step-exposure, roughness persists as shown in **Figure 15** after development in 0.26 mol L<sup>-1</sup> TMAH and rinse in water. The root-mean-square (RMS) roughness, determined by atomic force microscopy, is plotted versus the LILS take at the point of solubility. The two quencher cases discussed here and an additional case where the quencher is added to the acid-feeder layer for a coupled acid-base diffusion<sup>[35]</sup> are shown. The uniform and model photodegradable base cases always lead to a larger LILS and lower roughness when compared to no base. However, the roughness is not zero, but plateaus near 1.5 nm. While additives provide a route to achieve smaller dimensions by controlling the photoacid diffusion length, the persistent increase in LILS is saturated. Alternative strategies, such as incorporating amines within the backbone or even as a photo decomposable base would provide a test of the effect of base counter-diffusion by limiting segregation and mobility of the base that may increase, or decrease LWR/LER.<sup>[59]</sup>

### 3.5. Buried Lateral Structure

The diffuse reaction-diffusion profile measured by specular neutron reflectivity is averaged along the  $xy$ -plane as a function of diffusion/reaction depth, or thickness,  $z$ . Therefore, one averages out the in plane compositional fluctuations to achieve the profile, so a profile of a smooth gradient or composition-

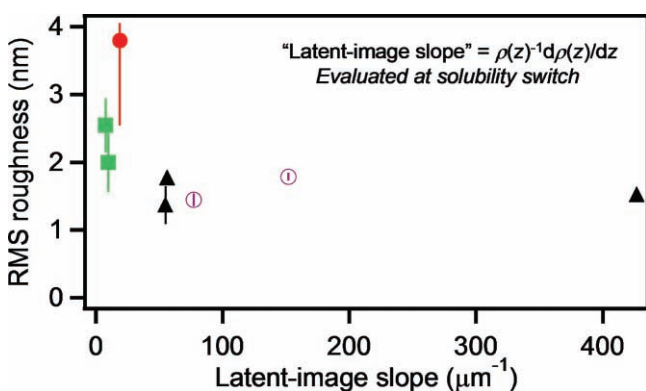


**Figure 15.** RMS roughness of developed bilayers as determined by SPM for different base locations: (●) no base, (■) coupled acid-base, (▼) uniform base, (▲) model photobase. As the latent image slope increases, there is an improvement in the RMS roughness to a finite limit of approximately 1.5 nm. Reprinted with permission from.<sup>[35]</sup> Copyright 2007, American Institute of Physics.

ally heterogeneous one, as shown in the schematic of **Figure 5**, may not be distinguishable by specular neutron reflectivity alone. The form of latent image roughness and relative location near the solubility switch may contribute to the final line-edge roughness. The lithographic line-edge roughness is only revealed after development. Therefore, whether the observed roughness is a direct transfer of latent image roughness or contains contributions from the development kinetics has been challenging to answer experimentally. In the following we will demonstrate that the in-plane compositional heterogeneous structure can be characterized via the diffuse scattering or off-specular reflectivity.

The specular neutron reflectivity results are shown in **Figure 16** for the deuterated model EUV photoresist poly(*d*-tertbutylacrylate-co-hydroxystyrene).<sup>[60,61]</sup> The deprotection reaction leads to volatile deuterated isobutene so that the deprotection profile can be determined with nanometer resolution.

The off-specular neutron reflectometry<sup>[32,33,62–65]</sup> method examines the diffuse scattering around the specular reflection peak by measuring a component of the scattering wave vector parallel ( $q_x$  in the plane of the beam) to the substrate. Off-specular transverse scans were performed at two different  $q_z$  values, 0.022 Å<sup>-1</sup> and 0.055 Å<sup>-1</sup> of **Figure 16** that provides sensitivity to lateral length scales from  $\approx$  100 nm to several micrometers.

The diffuse scattering was analyzed using a modified distorted-wave Born approximation.<sup>[32,33]</sup> While the form of Equation (3) describes the in-plane correlations, the contributions to the interfacial width were separated into a gradient in composition ( $\sigma_G$ ) and physical roughness ( $\sigma_R$ ). Assuming these terms are not coupled, they can be related in quadrature to the width obtained from specular reflectivity,

$$\sigma_{\text{Spec}}^2 = \sigma_G^2 + \sigma_R^2 \quad (7)$$

This provides a methodology to separate the gradual change in the deprotection extent from inhomogeneities at the reaction front.

The off-specular transverse scans at a  $q_z = 0.022$  Å<sup>-1</sup> after the PEB reaction are shown in **Figure 17** along with fits (lines) using the modified distorted-wave Born approximation.<sup>[32,33]</sup> Based upon the calculations of the diffuse scattering, if the entire 7.9 nm interfacial width is modeled by an inhomogeneous chemical roughness, the dotted line overestimates the diffuse scattering data. In the other extreme, if the reaction front is modeled as a smooth decrease in the deprotection extent with a flat wave front with no in-plane structure, the dashed line underestimates the diffuse scattering. The best fit was obtained by a combination of these extremes, whereby the deprotection extent is a physically rough front with a gradient component. This is shown as the solid line that is a result of a profile with a gradient over the first 7.5 nm and an inhomogeneous, low-amplitude roughness within the last 2.5 nm as shown superimposed on the specular and deprotection profile of **Figure 17**.

These measurements demonstrate that the buried physical roughness is well beyond the point of development shown as the dotted line. Therefore, the solubility switch point (deprotection level  $\approx$  0.2) is within the profile that is homogeneous with a sharp deprotection slope and not near the low-amplitude

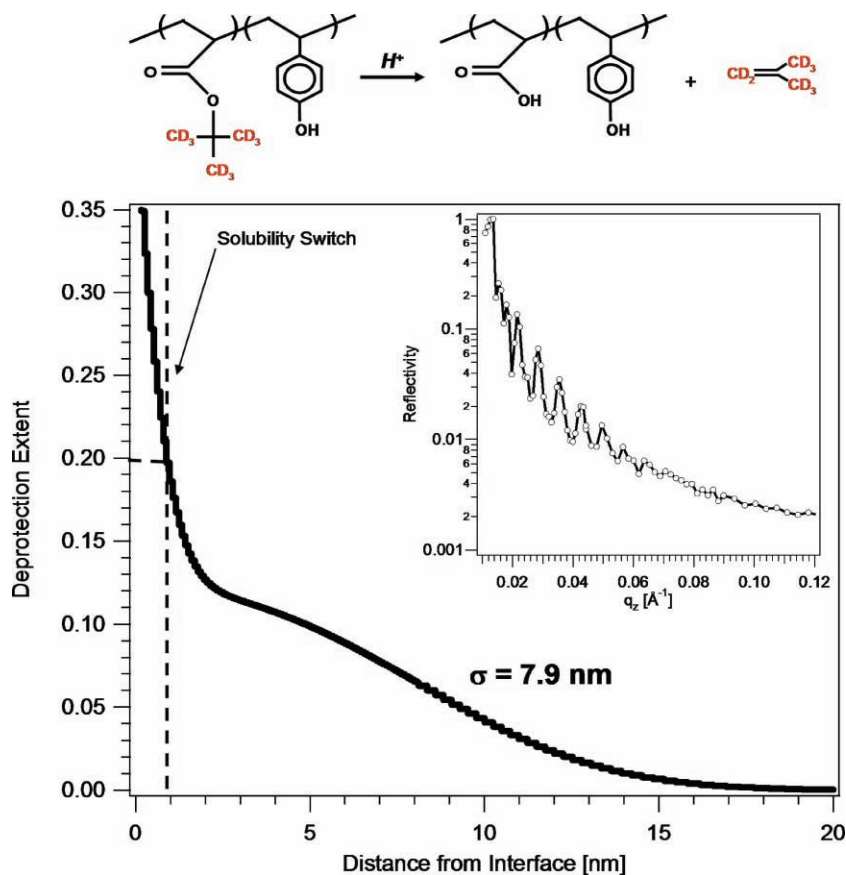


**Figure 16.** Deprotection profile from specular neutron reflectivity (inset) for the model EUV photoresist after post-exposure bake of 130 °C for 180 s. The solubility switch of deprotection level  $\approx 0.20$  is shown by the dotted line and interfacial width is 7.9 nm. Reprinted with permission.<sup>[61]</sup> Copyright 2008, American Institute of Physics.

roughness ( $\sigma_R$ ). Hence, the zone of buried compositional roughness is not transferred to the resist. Further, the buried lateral length scale ( $\xi$ ) was 800 nm, thus of lower frequency compared to the roughness of concern for lithographic feature quality, which is of the order of 100 nm to 200 nm.

Off-specular reflectivity highlights the structure of the buried deprotection reaction-diffusion front in a model EUV photoresist copolymer. These measurements show the latent image possesses a low-amplitude, low-frequency inhomogeneity at the leading edge of the reaction front. This inhomogeneity occurs at depth beyond the solubility switch for the resist in  $0.26 \text{ mol L}^{-1}$  TMAH and may diminish the role on line-edge roughness.

#### 4. Photoresist/Developer Interface

A central assumption in resolution limit models such as those described in Table I is the direct transfer of the chemical deprotection heterogeneity on the feature quality. The chemical and physical heterogeneity are transferred to the final feature after a threshold of the deprotection level. Therefore, the development process and mechanisms are not considered. However, it is known that partial dissolution of thin photoresist polymer films, such as poly(hydroxystyrene), leads to roughness as described

by the critical ionization model.<sup>[66]</sup> The bulk development of photoresist thin films dissolve via reactive-dissolution kinetics.<sup>[67–69]</sup> In this process, summarized by Hinsberg et al., the chemical equilibrium (acid-base reaction) between weakly acidic polymer functional groups and the strong aqueous base induces a switch in solubility. The ionization of the polymer photoresists leads to a polyelectrolyte in the developer solution (Figure 18b). The kinetics of the aqueous base hydroxide transport and the acid-base solution reaction controls the kinetics of formation of the steady-state gel layer that propagates with a well-defined thickness as the film dissolves. In general, a variety of non-analytic film dissolution kinetics may result depending upon the reactivity, kinetics parameters, and film mechanical properties of this photoresist development process.<sup>[29]</sup>

The propagating swollen layer of the dissolution front must approach the nominally unreacted and unexposed zone transitioning from bulk development into an interfacial process.<sup>[29]</sup> This transition-zone width is partly controlled by the reaction-diffusion process described previously. However, the spatial extent of swelling, transport of developer within the undeveloped transition zone, role of subsequent water rinse, and mechanism of drying are measurement challenges primarily due to the lack of readily accessible experimental methods.

This was addressed by contrast variant neutron reflectivity techniques that directly measured the developer penetration and extent of line-edge swelling.<sup>[70–72]</sup> A residual swelling fraction at the feature edge remains diffuse over length scales ( $>10 \text{ nm}$ ) that far exceeds the polymer chain dimensions during hydroxide development. The polymer remains swollen during the water rinse step and eventually collapses upon drying. Alternative development approaches to control this residual swelling fraction may be needed to smooth and reduce LER. Since, it is known that photoresists are polyelectrolytes<sup>[73]</sup> in developer solutions one expects counterion correlations to the polymer chain<sup>[74]</sup> and therefore the tetramethylammonium ions were measured using deuterium substitution.

#### 4.1. Contrast Variant Neutron Reflectivity at Solid/Liquid Interfaces

The acid feeder layer/photoresist polymer bilayer films were prepared with one slight modification to that described earlier; an antireflective (for visible light) coating (ARC) was applied to improve the adhesion of the photoresist polymer to the silicon substrate for the in situ development studies. Therefore, the trilayer is used for in situ development as shown in Figure 18a. The dry trilayer sample was characterized by neutron reflectivity on unexposed and post-exposure baked samples.<sup>[34]</sup>

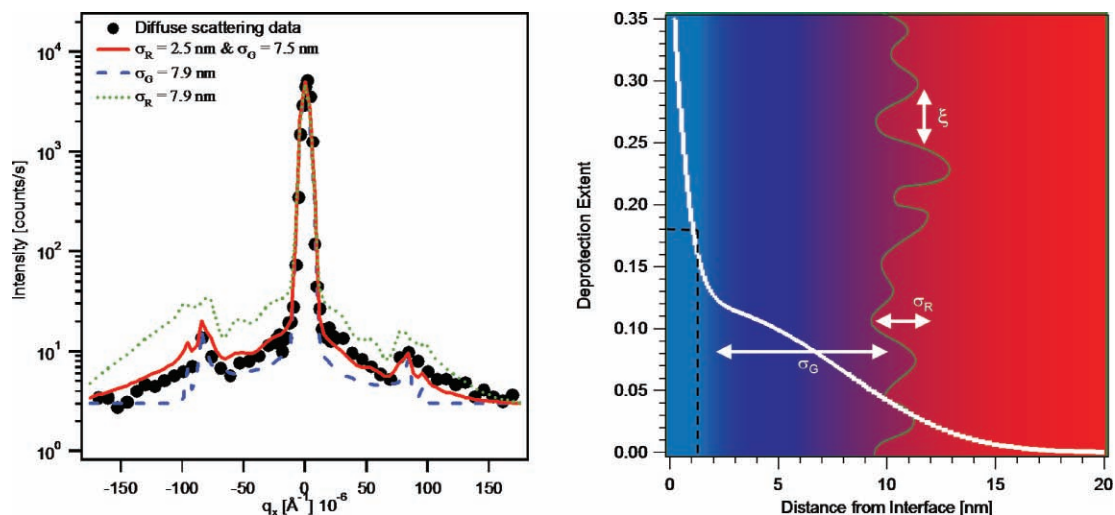


**Figure 17.** Off-specular transverse scan at  $q_z$  of  $0.022 \text{ \AA}^{-1}$  with calculations for a rough interface (dotted), a smooth gradient interface (dashed), and a combination of the two (solid).  $q_x$  spans from  $-0.000191 \text{ \AA}^{-1}$  to  $0.000191 \text{ \AA}^{-1}$ . Reprinted with permission.<sup>[61]</sup> Copyright 2008, American Institute of Physics.

Development was performed on the well-defined latent image reaction fronts using a custom liquid cell and a single sample was subject to in situ development and rinse. Two different trilayer samples were measured to characterize the polymer segmental profile and the deuterium labeled tetramethylammonium profile using a full contrast and zero-average contrast approach, respectively.<sup>[75]</sup> In order to maximize the scattering length contrast between hydrogenated polymer and the developer and rinse solutions, full contrast experiments used protonated  $0.065 \text{ mol L}^{-1}$  tetramethylammonium hydroxide (TMAH) in  $\text{D}_2\text{O}$ . After the deuterated developer was introduced into the cell, the acid feeder layer and portion of the reaction front dissolved. The film remaining in contact with the developer and was measured by specular neutron reflectivity (Figure 18c). Subsequently, the developer was removed from the cell, rinsed and filled with pure  $\text{D}_2\text{O}$  to mimic the rinse step.

A zero-average contrast experiment used a  $\text{D}_2\text{O}/\text{H}_2\text{O}$  mixture that matches the average scattering length density of the dry polymer film to the solvent. This is a contrast-matched experiment. Then by using  $0.065 \text{ mol L}^{-1}$  deuterium labeled  $d_{12}$ -tetramethylammonium ( $d$ -TMA) hydroxide the concentration profile of  $d$ -TMA can be determined in a single experiment. By combining the two types of measurement the composition profiles of polymer,  $d$ -TMA counterion, and solvent are determined with nanometer resolution.

#### 4.2. Shape of the Developer Front

In Figure 19a the in situ deprotection profile is shown along with the solubility switch. However, beyond the nominal solubility switch the developer penetrates and induces swelling. The volume fraction profiles ( $\phi_i$ ) for each component are plotted as  $\phi_i$  versus distance from the ARC/resist interface in Figure 19b. The polymer segment profile resolves the dense non-swollen region and transition to the residual swelling fraction. Concentrated phases ( $\phi \approx 1$ ) to semidilute and dilute regimes

are observed by these profiles, whereby the long tail in polymer concentration occurs in a dilute-solution regime assuming a homogeneous phase. This implies that these lipophilic, low-molecular-weight polymers associate to form the swollen line edge reminiscent of associating polymers. In such a case, the entropy gained by dissolving into the solution cannot overcome the association energy due to the hydrophobicity. Due to the lipophilic nature of the resulting polymers the size scale of the swelling structures survive the swelling stress.

The lower composition limit for swelling from the polymer segment profile was estimated to be 0.095 volume fraction of MAA from the latent image. This swelling limit is lower than that for a film in the absence of the deprotection gradient. In the single layer case the initial photoacid distribution is uniform and the deprotection process leads to chemically heterogeneous films, which at low deprotection extents are comprised of well-separated deprotection domains.<sup>[76]</sup> These diffuse deprotection domains percolate and overlap with longer post-exposure bake reaction time.<sup>[55]</sup> The percolation of MAA domains was correlated with the onset of swelling. However, at the feature line-edge the photoacid diffusion will lead to a highly connected or percolated structure as the photoacid follows multiple diffusion paths defined by the protected and deprotected species.<sup>[28]</sup> The resulting broad interface completely dissolves at the solubility switch, but water and developer will swell to the lower composition limit (0.095 volume fraction MAA). Below this deprotection level, water and developer are effectively excluded. This may arise from randomly distributed MAA groups leading to films that are too hydrophobic to allow unfavorable water–MAAdMA contacts. Alternatively, the hydrophilic MAA may be non-uniformly distributed into isolated pockets<sup>[77]</sup> or channels,<sup>[78,79]</sup> such that, while water can find a pocket of hydrophilic moieties, the surrounding stiff hydrophobic matrix prevents volume expansion.

In addition to the polymer, the  $d$ -TMA profiles achieve a peak concentration of 5% by volume and are enriched over the bulk volume fraction (0.55% by volume) because of the high concentration of weakly acidic MAA groups within the residual

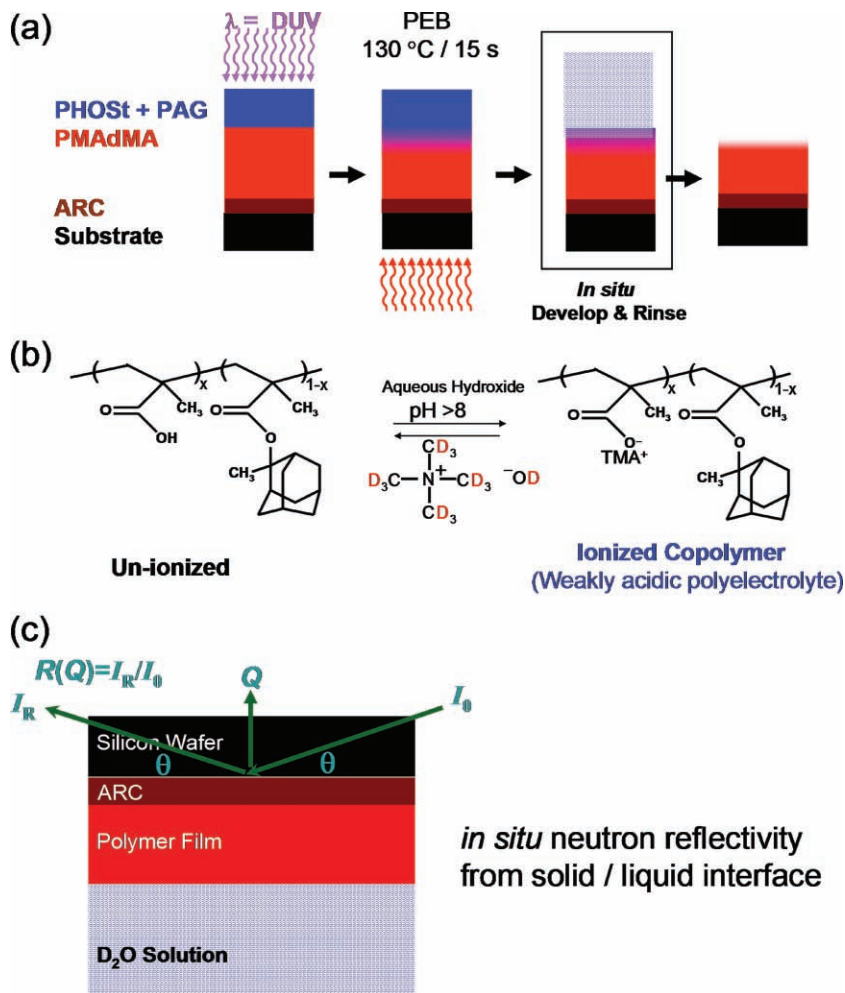


**Figure 18.** Modification of the in situ resist/developer interface study by neutron reflectivity. a) Inclusion of a thin ARC layer to improve adhesion and perform an in situ development and rinse experiment. b) Chemical equilibrium shifts the photoresist from neutral to polyelectrolyte; a deuterium labeled developer provides neutron contrast. c) Experimental geometry of specular neutron reflectivity through the silicon wafer substrate.

swelling fraction. The process by which *d*-TMA is enhanced is partially due to the local titration of the high concentration of MAA segments, while the decay of *d*-TMA to the bulk is expected by the low concentration of polymer segments, as well as dilute bulk solution concentrations.

The in situ water rinse of Figure 19c shows the persistence of swelling. In the present case the MAA, a hydrophilic moiety, ionizes in water as demonstrated in model polyelectrolyte systems such as brushes and gels. In the present case both the developer and water rinse may be regarded as good solvents. In previous photoresist generations, such as those incorporating hydroxystyrene, water should be a poor solvent, since poly(hydroxystyrene) is not water soluble. Therefore, the collapse should occur more prominently during the water rinse step.

Lastly, the swollen region collapses after drying (Figure 19d) thereby converting a diffuse swollen rinse interface into a surface with roughness of only 7 nm. Therefore, the roughening at the interface contributes to a non-ideal film collapse. This final roughness may limit future device scaling, therefore alternate

materials strategies may be required if chemically amplified photoresists are to be used for sub-22-nm features. These measurements support a mechanism that resist polymer chains may rearrange in a dilute swollen phase, as well as further segregate to the surface. The non-ideal collapse can cause segregation of polymer groups based on relative hydrophobicity, or possibly through the film drying mechanism. Controlling the swelling and collapse via polymer chemistry, solvent quality, and molecular weight remains a crucial area of interest with regards to these chemical-gradient interfaces.

The significance of these results rests in the length scales of swelling and in that a large fraction of the deprotected interface swells, but does not dissolve. These measurements challenge the mechanism for development that do not include the gradient in deprotection, nor the polymer physics of swelling. Further, the length scale of swelling exceeds the size of the polymer molecules used. Therefore, the structure of the deprotection plays a role in both the onset of photoresist dissolution and the ability to balance the swelling stress in the form of associating behavior.

Figure 20 shows that the spatial extent of swelling at the line edge will impact the ultimate resist resolution as the feature space approaches the characteristic swelling length. In this reconstructed line and space feature, using the data from Figure 19, swelling occurs in both the development and water rinse process. In this system, the swelling layers would touch at  $\approx 80$  nm space and overlap at  $\approx 45$  nm space. The drying process of the swelling layers may be a critical source of defects in photoresists that result in microbridging.<sup>[80,81]</sup> The dense swelling layers could also contribute to a lateral force that leads to instabilities and line collapse. Advanced resist materials that reduce the swelling spatial extent by control over the molecular weight or rinse additives should be considered in light of these observations.

In contrast, a negative-tone photoresist such as calixarene derivatives has been demonstrated to produce 12.5 nm half-pitch resolution.<sup>[82]</sup> In this case the development of the low-molar-mass precursors may reduce swelling due to the high crosslink density. Traditional positive-tone electron beam resist such as PMMA undergoes chain scission; therefore the fragmentation at the exposed region is the source of development contrast. A combination of main-chain scission with chemical amplification would reduce the swelling extent by eliminating the susceptibility of association<sup>[83]</sup> due to the molecular-weight contrast, rather than lipophilic contrast. Materials are being redesigned based on lessons from electron beam resists<sup>[84]</sup> and may lead to efficient routes to control both the reaction diffusion and swelling length scales.

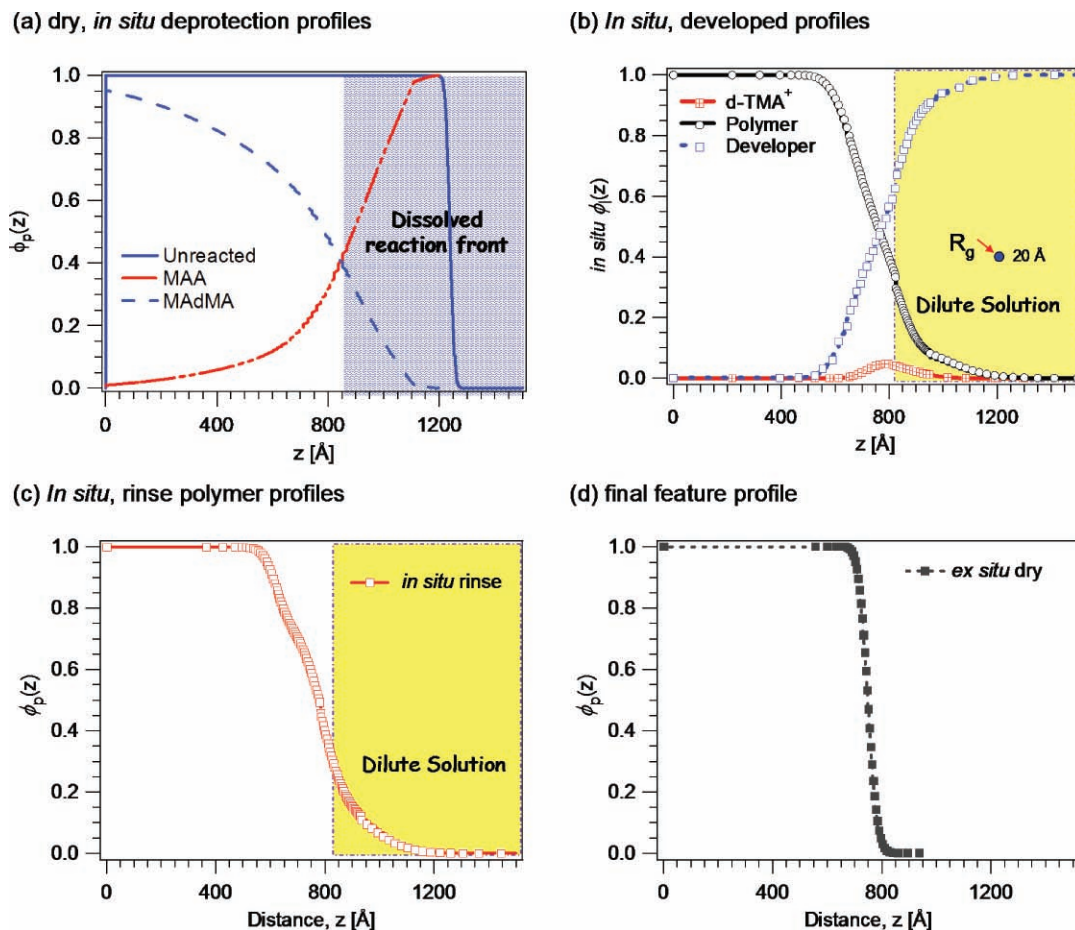


**Figure 19.** Systematic measurements of a) dry, *in situ* deprotection profiles, b) *in situ* development profiles, c) polymer profile during water rinse, and d) final physical profile of the developed feature. Neutron reflectivity demonstrates that a diffuse swelling front precedes the final feature through a swelling-layer collapse mechanism. Adapted with permission.<sup>[70]</sup> Copyright 2007, American Institute of Physics.

## 5. Advances by Material Structure

In a typical polymer photoresists the PAG is dissolved along with the polymer and spin cast to form a thin film mixture, or binary blend. Polymers provide flexible platforms to change functional groups in order to meet etch resistance, optical transparency, refractive index requirements, and a variety of acid-sensitive protecting groups. The high glass-transition temperatures (typically,  $T_g > 140$  °C) provide dimensional stability and a wide latitude in post-exposure bake temperature that increases the rates of reaction and photoacid diffusivity. Finally, polymers have a large degree of lipophilicity in an aqueous base developer that provides a high development contrast.<sup>[9]</sup>

Reducing the photoacid diffusion length would enable smaller features or higher resolution, however, the PAG and photoresist polymer-blend approach may not be the most effective route, since the photoacid could diffuse to lengths longer than the CD. In order to address this concern, an alternative resist structure was devised that covalently bonds the photoacid generator to the polymer as shown in **Figure 21a**.<sup>[85–88]</sup> With this approach, after exposure, the photoacid counter-anion remains covalently bound to the polymer thereby restricting the acidic proton diffusion length.

Since the CD and LER metrics are approaching the characteristic dimensions of the photoresist polymers, alternative architectures were considered to extend photolithography by using lower-molar-mass molecules.<sup>[89]</sup> These molecular resists, while smaller, may also improve the uniformity of blends with PAGs and other additives, since miscibility of polymer blends decreases with increasing molar mass.<sup>[90]</sup> In general the molecular glass resist has a well-defined small-molecule core that bears protected base-soluble groups (such as hydroxyls and carboxyls) as shown in **Figure 21b**. With this approach the core chemistry can vary from calix[4]resorcinarenes (ringlike),<sup>[91–93]</sup> branched phenolic groups,<sup>[94,95]</sup> and hexaphenolic groups (disklike).<sup>[96,97]</sup>

Early approaches with molecular resists led to low glass-transition temperatures, however, such problems were resolved by increased hydrogen bonding functionality and the design of the core structure. These molecular resists may also benefit from a more uniform development due to the lack of chain entanglements and reduced swelling, when compared to polymers; these are active areas of research. Most of these alternative resist structures adhere to the chemical amplification strategy. However, nonchemically amplified photoresists are also being considered

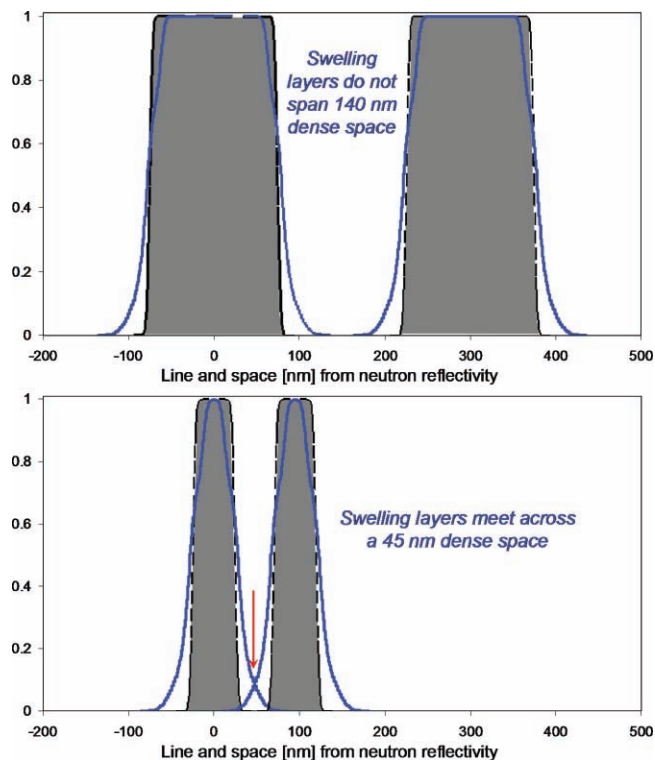


**Figure 20.** Dense line and space structure of the water rinse swollen feature (solid line) and dried feature (filled) reconstructed using the profiles from Figure 19c and d, respectively. The volume fraction of swelling photoresist polymer do not touch at large spaces, but at 45 nm space the swelling layers touch and overlap and impact device defects, roughness, and microbridging.

as they do not contain photoacid generators and hence do not suffer from photoacid diffusion length constraints.<sup>[98]</sup>

Two other novel variants are PAG covalently bound to the molecular resist (Figure 21c) or the core of the molecule

serving as the PAG<sup>[99]</sup> (Figure 21d). As designed, there would be no need for blending of PAG with such resist systems. In the case of Figure 21d photolysis produces a photoacid, which then deprotects the unexposed acid-sensitive protecting groups of the PAG-core molecular glass. These two approaches (Figure 21c and d) are also smaller pixel sizes and true one-component systems that in principle eliminate surface segregation and phase separation in cast films. The quantitative measurements of basic photoacid diffusion length, LILS, and dose sensitivity are currently under investigation. However, as observed with polymers, additives such as amine base quenchers may be required to limit diffusion of the photoacid.

## 6. Conclusions

A measurement platform based on X-ray and neutron reflectivity was developed to determine and test the relationships between polymer photoresist materials chemistry and formulation and the underlying chemical reaction-diffusion process and reactive-dissolution mechanism. Overall, the feature fidelity requires control at all levels of photoresist formulations and processing. In addition to meeting photoresist materials design guidelines, especially the transparency of the resists that changes with each successive technological node or exposure wavelength, the spatial extent of reaction must be controlled at a level finer than the expected critical dimension. Such a conclusion is quite obvious; the measurements outlined here provide a high-resolution picture of how resist chemistry, photoacid generator size, processing time, and temperature contribute to the reaction-diffusion and image blur. Further, the use of off-specular neutron reflectivity can be used to probe the three-dimensional structure of thin-film interfaces and the application has identified that buried reaction-diffusion fronts possess smooth compositional gradients, i.e., no detectable lateral compositional heterogeneity, near the solubility switch site.

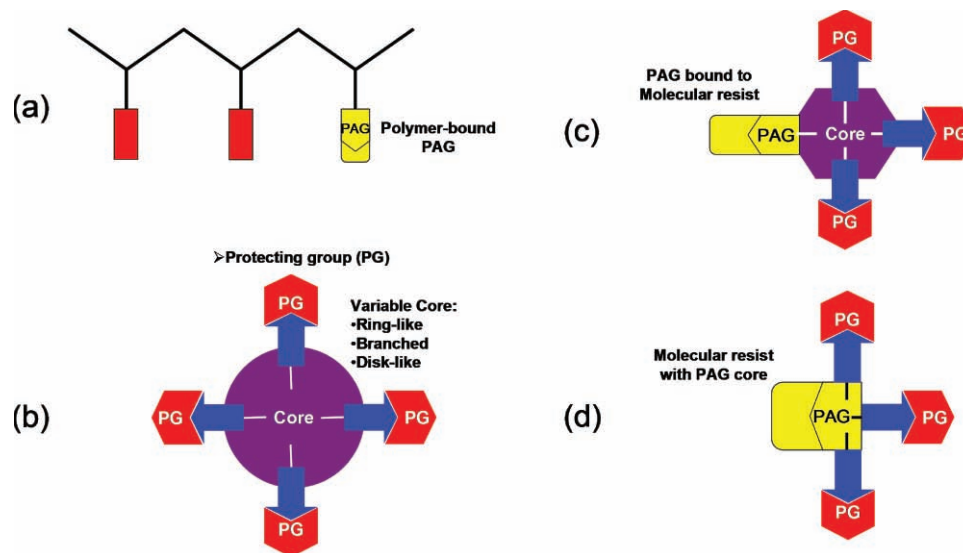


**Figure 21.** Cartoons of photoresist architecture alternative to polymer and PAG blends: a) Photoresist polymer bound to the PAG, b) molecular glass resist with variable core structure, c) molecular glass resist bound to the PAG, and d) PAG-core molecular resist.

This, in turn, suggests that new development strategies may be the only effective route to improve the LER in current photoresist materials.

Finally, for the first time, neutron reflectivity has brought some understanding of how swelling during development relates to resolution and LER. Materials that swell to spatial extents of the order of the line/space is expected to encounter problems. Again, the swelling length scales were measured and the results indicate that the reduction of swelling can be quantified. This opens the possibility that a direct comparison between the lithographic results and the magnitude of swelling can be made. Besides neutron reflectivity, very few measurements are capable of directly measuring the nanometer-scale swelling at diffuse soft interfaces. Neutron and perhaps X-ray reflectivity can play a more active role to understand materials dissolution for technological applications. In light of traditional polymer photoresists, the role of smaller molecular resists is an emerging area of activity. The observations made here highlight that simultaneously controlling the reaction front and developer front are important. The use of smaller molecules that can not support a swelling stress could address specific issues such as swelling and collapse on feature fidelity.

## Acknowledgements

This work was supported by Sematech under Agreement #309841 OF and a cooperative research and development agreement between Intel Corporation and NIST (NIST CRADA #CN-1892 and 1893). We acknowledge Karen Turnquest from Sematech and Kwang-Woo Choi, Manish Chandhok, Wang Yueh, Todd Younkin, Steve Putna, George Thompson, and Christof Krautschik from Intel for their input and support. In particular, special thanks go to Bryan Vogt (Arizona State University), Kristopher Lavery (Qualcomm), and Ashwin Rao (Rhodia) for their technical contributions over the years. Certain commercial equipment and materials are identified in this paper in order to specify adequately the experimental procedure. In no case does such identification imply recommendations by the National Institute of Standards and Technology nor does it imply that the material or equipment identified is necessarily the best available for this purpose. Official contribution of the National Institute of Standards and Technology; not subject to copyright in the United States. This article is part of a Special Issue on Materials Science at the National Institute of Standards and Technology (NIST).

Received: May 12, 2010

Published online: September 16, 2010

- [1] H. J. Levinson, *Principles of Lithography*, 2nd ed. SPIE Press, Bellingham, Washington, 2005.
- [2] M. Chandhok, S. Datta, D. Lionberger, S. Vesecky, *Proc. SPIE* **2007**, 6519, 65191A-1.
- [3] <http://public.itrs.net>, International Technology Roadmap for Semiconductors **2007**, (accessed Sept. 2009).
- [4] H. Ito, C. G. Willson, *Polym. Eng. Sci.* **1983**, 23, 1012.
- [5] H. Ito, C. G. Willson, *ACS Symp. Ser.* **1984**, 242, 11.
- [6] G. M. Wallraff, W. D. Hinsberg, *Chem. Rev.* **1999**, 99, 1801.
- [7] W. Hinsberg, F. A. Houle, J. Hoffnagle, M. Sanchez, G. Wallraff, M. Morrison, S. Frank, *J. Vac. Sci. Technol. B* **1998**, 16, 3689.
- [8] A. Pawloski, A. Acheta, I. Lalovic, B. LaFontaine, H. Levinson, *Proc. SPIE* **2004**, 5376, 414.
- [9] H. Ito, *Adv. Polym. Sci.* **2005**, 172, 37.
- [10] H. Ito, *J. Polym. Sci., Part A: Polym. Chem.* **2003**, 41, 3863.
- [11] C. G. Willson, H. Ito, J. M. J. Frechet, T. G. Tessier, F. M. Houlihan, *J. Electrochem. Soc.* **1986**, 133, 181.
- [12] F. A. Houle, W. D. Hinsberg, M. I. Sanchez, J. A. Hoffnagle, *J. Vac. Sci. Technol. B* **2002**, 20, 924.
- [13] T. Kozawa, S. Tagawa, J. J. Santillan, M. Toriumi, T. Itani, *J. Vac. Sci. Technol. B* **2007**, 25, 2295.
- [14] J. H. Kim, Y. H. Kim, S. M. Chon, T. Nagai, M. Noda, Y. Yamaguchi, Y. Makita, H. Nemoto, *J. Photopolym. Sci. Technol.* **2004**, 17, 379.
- [15] G. M. Schmid, M. D. Stewart, V. K. Singh, C. G. Willson, *J. Vac. Sci. Technol. B* **2002**, 20, 185.
- [16] M. D. Stewart, H. V. Tran, G. M. Schmid, T. B. Stachowiak, D. J. Becker, C. G. Willson, *J. Vac. Sci. Technol. B* **2002**, 20, 2946.
- [17] J. A. Hoffnagle, W. D. Hinsberg, M. I. Sanchez, F. A. Houle, *Opt. Lett.* **2002**, 27, 1776.
- [18] D. L. VanderHart, V. M. Prabhu, A. De Silva, N. M. Felix, C. K. Ober, *J. Mater. Chem.* **2009**, 19, 2683.
- [19] D. L. VanderHart, V. M. Prabhu, E. K. Lin, *Chem. Mater.* **2004**, 16, 3074.
- [20] D. L. VanderHart, V. M. Prabhu, K. L. Lavery, C. L. Dennis, A. B. Rao, E. K. Lin, *J. Magn. Reson.* **2009**, 201, 100.
- [21] G. M. Gallatin, P. Naulleau, D. Niakoula, R. Brainard, E. Hassanein, R. Matyi, J. Thackeray, K. Spear, K. Dean, *Proc. SPIE* **2008**, 6921, 69211E-1.
- [22] R. L. Bristol, *Proceedings of SPIE* **2007**, 6519, 65190W-1.
- [23] D. Van Steenwinkel, R. Gronheid, J. H. Lammers, A. M. Meyers, F. Van Roey, P. Willems, *Proc. SPIE* **2007**, 6519, 65190V-1.
- [24] R. Brainard, E. Hassanein, J. Li, P. Pathak, B. Thiel, F. Cerrina, R. Moore, M. Rodriguez, B. Yakshinskiy, E. Loginova, T. Madey, R. Matyi, M. Malloy, A. Rudack, P. Naulleau, A. Wuest, K. Dean, *Proc. SPIE* **2008**, 6923, 692325-1.
- [25] G. M. Gallatin, *Proc. SPIE* **2004**, 5754, 38.
- [26] G. M. Gallatin, P. Naulleau, R. Brainard, *Proc. SPIE* **2007**, 6519, 651911-1.
- [27] T. H. Fedynshyn, R. B. Goodman, J. Roberts, *Proc. SPIE* **2008**, 6923, 692319-1.
- [28] F. A. Houle, W. D. Hinsberg, M. Morrison, M. I. Sanchez, G. Wallraff, C. Larson, J. Hoffnagle, *J. Vac. Sci. Technol. B* **2000**, 18, 1874.
- [29] F. A. Houle, W. D. Hinsberg, M. I. Sanchez, *Macromolecules* **2002**, 35, 8591.
- [30] S. Kang, W. L. Wu, V. M. Prabhu, B. D. Vogt, E. K. Lin, K. Turnquest, *Proc. SPIE* **2007**, 6159, 65193V-1.
- [31] E. K. Lin, C. L. Soles, D. L. Goldfarb, B. C. Trinquet, S. D. Burns, R. L. Jones, J. L. Lenhart, M. Angelopoulos, C. G. Willson, S. K. Satija, W. L. Wu, *Science* **2002**, 297, 372.
- [32] S. K. Sinha, E. B. Sirota, S. Garoff, H. B. Stanley, *Phys. Rev. B* **1988**, 38, 2297.
- [33] M. Wormington, I. Pape, T. P. A. Hase, B. K. Tanner, D. K. Bowen, *Philos. Mag. Lett.* **1996**, 74, 211.
- [34] B. D. Vogt, S. Kang, V. M. Prabhu, E. K. Lin, S. K. Satija, K. Turnquest, W. Wu, *Macromolecules* **2006**, 39, 8311.
- [35] B. D. Vogt, S. Kang, V. M. Prabhu, A. Rao, E. K. Lin, W. L. Wu, S. K. Satija, K. Turnquest, *J. Vac. Sci. Technol. B* **2006**, 25, 175.
- [36] B. D. Vogt, S. Kang, V. M. Prabhu, A. Rao, E. K. Lin, S. K. Satija, K. Turnquest, W. Wu, *Proc. SPIE* **2006**, 6153, 615316-1.
- [37] M. D. Stewart, M. H. Somervell, H. V. Tran, S. V. Postnikov, C. G. Willson, *Proc. SPIE* **2000**, 3999, 665.
- [38] G. Wallraff, J. Hutchinson, W. Hinsberg, F. Houle, P. Seidel, R. Johnson, W. Oldham, *J. Vac. Sci. Technol. B* **1994**, 12, 3857.
- [39] W. Hinsberg, G. Wallraff, F. Houle, M. Morrison, J. Frommer, R. Beyers, J. Hutchinson, *Org. Thin Films* **1998**, 695, 344.
- [40] W. Hinsberg, F. Houle, M. Sanchez, M. Morrison, G. Wallraff, C. Larson, J. Hoffnagle, P. Brock, G. Breyta, *Proc. SPIE* **2000**, 3999, 148.
- [41] W. D. Hinsberg, F. A. Houle, M. I. Sanchez, G. M. Wallraff, *IBM J. Res. Dev.* **2001**, 45, 667.

- [42] F. A. Houle, W. D. Hinsberg, M. I. Sanchez, *J. Vac. Sci. Technol. B* **2004**, *22*, 747.
- [43] S. Kang, V. M. Prabhu, B. D. Vogt, E. K. Lin, W. L. Wu, K. Turnquest, *Proc. SPIE* **2006**, *6153*, 61533N-1.
- [44] S. H. Kang, V. M. Prabhu, B. D. Vogt, E. K. Lin, W. L. Wu, K. Turnquest, *Polymer* **2006**, *47*, 6293.
- [45] X. L. Shi, *J. Vac. Sci. Technol. B* **1999**, *17*, 350.
- [46] S. Kang, V. M. Prabhu, W. L. Wu, E. K. Lin, K. W. Choi, M. Chandhok, T. R. Younkin, W. Yueh, *Proc. SPIE* **2009**, *7273*, 72733U-1.
- [47] S. Kang, K. Lavery, K. W. Choi, V. M. Prabhu, W. L. Wu, E. K. Lin, A. De Silva, N. Felix, C. Ober, *Proc. SPIE* **2008**, *6923*, 692317-1.
- [48] Y. Nishimura, T. B. Michaelson, J. E. Meiring, M. D. Stewart, C. G. Willson, *J. Photopolym. Sci. Technol.* **2005**, *18*, 457.
- [49] H. Momose, S. Wakabayashi, T. Fujiwara, K. Ichimura, J. Nakauchi, *Proc. SPIE* **2001**, *4345*, 695.
- [50] Y. Uetani, H. Fujishima, *Proc. SPIE* **2000**, *3999*, 974.
- [51] H. Ito, H. D. Truong, P. J. Brock, *Proc. SPIE* **2008**, *6923*, 692318-1.
- [52] W. L. Wu, V. M. Prabhu, E. K. Lin, *Proc. SPIE* **2007**, *6519*, 651902-1.
- [53] B. D. Vogt, C. L. Soles, C.-Y. Wang, V. M. Prabhu, P. M. McGuiggan, J. F. Douglas, E. K. Lin, W. Wu, S. K. Satija, D. L. Goldfarb, M. Angelopoulos, *J. Microlithogr., Microfabr., Microsyst.* **2005**, *4*, 013003.
- [54] www.semtech.org, (accessed September 2009).
- [55] S. Kang, B. D. Vogt, W. L. Wu, V. M. Prabhu, D. L. VanderHart, A. Rao, E. K. Lin, K. Turnquest, *Macromolecules* **2007**, *40*, 1497.
- [56] S. Kang, B. D. Vogt, W. L. Wu, V. M. Prabhu, D. L. VanderHart, A. Rao, E. K. Lin, K. Turnquest, *Proc. SPIE* **2007**, *6159*, 615916-1.
- [57] A. R. Pawloski, A. Acheta, H. J. Levinson, T. B. Michaelson, A. Jamieson, Y. Nishimura, C. G. Willson, *J. Microlithogr. Microfabr. Microsyst.* **2006**, *5*, 023001.
- [58] S. V. Postnikov, M. D. Stewart, H. V. Tran, M. A. Nierode, D. R. Medeiros, T. Cao, J. Byers, S. E. Webber, C. G. Wilson, *J. Vac. Sci. Technol. B* **1999**, *17*, 3335.
- [59] F. M. Houlihan, D. Rentkiewicz, G. Lin, D. Rahman, D. Mackenzie, A. G. Timko, T. Kudo, C. Anyadiiegwu, M. Thiyagarajan, S. Chiu, A. Romano, R. R. Dammel, M. Padmanaban, *Proc. SPIE* **2006**, *6153*, 615317-1.
- [60] K. A. Lavery, B. D. Vogt, V. M. Prabhu, E. K. Lin, W. L. Wu, S. K. Satija, K. W. Choi, *J. Vac. Sci. Technol. B* **2006**, *24*, 3044.
- [61] K. A. Lavery, V. M. Prabhu, E. K. Lin, W. L. Wu, S. K. Satija, K. W. Choi, M. Wormington, *Appl. Phys. Lett.* **2008**, *92*, 064106.
- [62] L. Nevot, P. Croce, *Rev. Phys. Appl.* **1980**, *15*, 761.
- [63] W. L. Wu, *J. Chem. Phys.* **1993**, *98*, 1687.
- [64] V. Holy, T. Baumbach, *Phys. Rev. B* **1994**, *49*, 10668.
- [65] Y. Yoneda, *Phys. Rev.* **1963**, *131*, 2010.
- [66] P. C. Tsiartas, L. W. Flanagan, W. D. Hinsberg, C. L. Henderson, I. C. Sanchez, R. T. Bonnecaze, C. G. Willson, *Macromolecules* **1997**, *30*, 4656.
- [67] W. Hinsberg, F. A. Houle, S. W. Lee, H. Ito, K. Kanazawa, *Macromolecules* **2005**, *38*, 1882.
- [68] W. D. Hinsberg, F. A. Houle, H. Ito, K. Kanazawa, S. W. Lee, *Proc. 13th Int. Conference on Photopolymers, Advances in Imaging Materials and Processes, RETEC* **2003**, 193.
- [69] W. D. Hinsberg, F. A. Houle, H. Ito, *Proc. SPIE* **2004**, *5376*, 352.
- [70] V. M. Prabhu, B. D. Vogt, S. Kang, A. Rao, E. K. Lin, S. K. Satija, *J. Vac. Sci. Technol. B* **2007**, *25*, 2514.
- [71] V. M. Prabhu, B. D. Vogt, S. Kang, A. Rao, E. K. Lin, S. K. Satija, K. Turnquest, *Proc. of SPIE* **2007**, *6519*, 651910-1.
- [72] V. M. Prabhu, A. Rao, S. Kang, E. K. Lin, S. K. Satija, *J. Phys. Chem. B* **2008**, *112*, 15628.
- [73] V. M. Prabhu, R. L. Jones, E. K. Lin, W. L. Wu, *J. Vac. Sci. Technol. B* **2003**, *21*, 1403.
- [74] V. M. Prabhu, *Curr. Opin. Colloid Interface Sci.* **2005**, *10*, 2.
- [75] V. M. Prabhu, B. D. Vogt, W. L. Wu, J. F. Douglas, E. K. Lin, S. K. Satija, D. L. Goldfarb, H. Ito, *Langmuir* **2005**, *21*, 6647.
- [76] A. Rao, S. Kang, B. D. Vogt, V. M. Prabhu, E. K. Lin, W. L. Wu, M. Muthukumar, *Langmuir* **2006**, *22*, 10009.
- [77] J. Meiring, T. B. Michaelson, A. Jamieson, Schmid GM, *Proceedings SPIE* **2005**, *5753*, 350.
- [78] R. Dammel, *Diazonaphthoquinone-based resists*, SPIE—The International Society for Optical Engineering, TT 11, Tutorial Text in Optical Engineering, **1993**.
- [79] J. P. Huang, T. K. Kwei, A. Reiser, *Macromolecules* **1989**, *22*, 4106.
- [80] B. Rathasack, K. Nafus, S. Hatakeyama, Y. Kuwahara, J. Kitano, R. Gronheid, A. V. Pret, *Proc. SPIE* **2009**, *7273*, 727347-1.
- [81] K. S. Patel, M. C. Lawson, P. R. Varanasi, D. R. Medeiros, G. M. Wallraff, P. J. Brock, R. A. DiPietro, Y. Nishimura, T. Chiba, M. Slezak, *Proc. SPIE* **2004**, *5376*, 94.
- [82] H. H. Solak, Y. Ekinci, P. Kaser, S. Park, *J. Vac. Sci. Technol. B* **2007**, *25*, 91.
- [83] C. Eschbaumer, N. Heusinger, M. Kern, A. Jutgla, C. Hohle, M. Sebald, *J. Photopolym. Sci. Technol.* **2003**, *16*, 13.
- [84] H. Ito, L. K. Sundberg, L. Bozano, E. M. Lofano, K. Yamanaka, Y. Terui, M. Fujiwara, *Proc. SPIE* **2009**, *7273*, 72733H-1.
- [85] M. X. Wang, K. E. Gonsalves, M. Rabinovich, W. Yueh, J. M. Roberts, *J. Mater. Chem.* **2007**, *17*, 1699.
- [86] M. X. Wang, C. T. Lee, C. L. Henderson, W. Yueh, J. M. Roberts, K. E. Gonsalves, *J. Mater. Chem.* **2008**, *18*, 2704.
- [87] Y. Fukushima, T. Watanabe, R. Ohnishi, H. Shiotani, S. Suzuki, M. Hayakawa, Y. Endo, T. Yamanaka, S. Yusa, H. Kinoshita, *Jap. J. Appl. Phys.* **2008**, *47*, 6293.
- [88] H. P. Wu, K. E. Gonsalves, *Adv. Funct. Mater.* **2001**, *11*, 271.
- [89] T. Hirayama, D. Shiono, H. Hada, J. Onodera, *J. Photopolym. Sci. Technol.* **2004**, *17*, 435.
- [90] D. L. VanderHart, A. De Silva, N. Felix, V. M. Prabhu, C. K. Ober, *Proc. SPIE* **2008**, *6923*, 69231M-1.
- [91] K. Young-Gil, J. B. Kim, T. Fujigaya, Y. Shibusaki, M. Ueda, *J. Mater. Chem.* **2002**, *12*, 53.
- [92] S. W. Chang, R. Ayothi, D. Bratton, D. Yang, N. Felix, H. B. Cao, H. Deng, C. K. Ober, *J. Mater. Chem.* **2006**, *16*, 1470.
- [93] D. Yang, S. W. Chang, C. K. Ober, *J. Mater. Chem.* **2006**, *16*, 1693.
- [94] A. De Silva, J. K. Lee, X. Andre, N. M. Felix, H. B. Cao, H. Deng, C. K. Ober, *Chem. Mater.* **2008**, *20*, 1606.
- [95] N. M. Felix, A. De Silva, C. M. Y. Luk, C. K. Ober, *J. Mater. Chem.* **2007**, *17*, 4598.
- [96] A. De Silva, N. Felix, J. Sha, J. K. Lee, C. K. Ober, *Proc. SPIE* **2008**, *6923*, 69231L-1.
- [97] A. De Silva, N. Felix, D. Forman, J. Sha, C. K. Ober, *Proc. SPIE* **2008**, *6923*, 69230O-1.
- [98] I. Nishimura, W. H. Heath, K. Matsumoto, W. L. Jen, S. S. Lee, C. Neikirk, T. Shimokawa, K. Ito, K. Fujiwara, C. G. Willson, *Proc. SPIE* **2008**, *6923*, 69231C-1.
- [99] R. A. Lawson, C. T. Lee, W. Yueh, L. Tolbert, C. L. Henderson, *Proc. SPIE* **2008**, *6923*, 69230K-1.